



1 **Interpreting Summertime Hourly Variation of NO₂ Columns with Implications for**
2 **Geostationary Satellite Applications**

3 Deepangsu Chatterjee¹, Randall V. Martin¹, Chi Li¹, Dandan Zhang¹, Haihui Zhu¹, Daven K. Henze²,
4 James H. Crawford³, Ronald C. Cohen^{4,5}, Lok N. Lamsal⁶, Alexander M. Cede⁶

5 ¹Department of Energy, Environmental & Chemical Engineering, Washington University in St. Louis, St.
6 Louis, MO, USA

7 ²Department of Mechanical Engineering, University of Colorado, Boulder, CO, USA

8 ³NASA Langley Research Center, Hampton, VA, USA

9 ⁴Department of Chemistry, University of California, Berkeley, Berkeley, CA, USA

10 ⁵Department of Earth and Planetary Science, University of California, Berkeley, Berkeley, CA, USA

11 ⁶NASA Goddard Space Flight Center, Greenbelt, MD 20771, USA

12

13 Correspondence: Deepangsu Chatterjee (deepangsuchatterjee@wustl.edu)

14

15 **Abstract**

16 Accurate representation of the hourly variation of the NO₂ column-to-surface relationship is needed to
17 interpret geostationary constellation observations of tropospheric NO₂ columns. Prior work has revealed
18 inconsistency in the hourly variation in NO₂ columns and surface concentrations. In this study, we use the
19 high-performance configuration of the GEOS-Chem model (GCHP) to interpret the daytime hourly
20 variation in NO₂ total columns and surface concentrations during summer. We use summer-time Pandora
21 sun photometers and aircraft measurements during the Deriving Information on Surface Conditions from
22 Column and Vertically Resolved Observations Relevant to Air Quality (DISCOVER-AQ) field campaign
23 over Maryland, Texas, and Colorado as well as 50 sites (31: contiguous USA, 10: Europe, 9: Asia) from
24 the Pandora Global Network (PGN). We correct the Pandora columns for 1) hourly variation in the column
25 effective temperature driven by the fractional boundary layer contribution to the total column, and 2) change
26 in local solar time along the line-of-sight of the Pandora instrument. The corrected Pandora observations
27 are increased by about $5\text{-}6 \times 10^{14}$ molecules cm⁻² at 9 AM and 6 PM across all Pandora sites. We conduct
28 fine resolution (~12 km) simulations over the contiguous US, Europe, and East Asia using the stretched
29 grid capability of GCHP. We also examine the effect of planetary boundary layer height (PBLH) corrections
30 on the total columns. We first evaluate the GCHP simulated absolute NO₂ concentration with Pandora and
31 aircraft observations. We find that fine resolution simulations at 12 km compared with moderate resolution
32 ~55 km reduce the Normalized Bias (NB) versus Pandora total columns (19% to 10%) and versus aircraft
33 measurements (25% to 13%) over Maryland, Texas, and Colorado. Fine resolution simulations at 12 km
34 compared with moderate resolution at 55 km reduce the NB versus Pandora total columns over the eastern
35 US (17% to 9%), western US (22% to 14%), Europe (24% to 15%), and Asia (29% to 21%). We next use
36 the 12 km simulation to examine the hourly variation in the NO₂ column and surface concentrations. We
37 explain the weaker hourly variation in NO₂ columns than at the surface as a function of 1) hourly variation
38 in the column effective temperature, 2) hourly variation in the local solar time along the Pandora line-of-
39 sight and 3) the integral of weakly connected layers; with the lowest 500 m exhibiting greater NO₂
40 concentrations in morning and evening than midday, while the residual column above 500 m dominates the
41 total column with weaker variability.

42

43



44 **1 Introduction**

45 Nitrogen oxides ($\text{NO}_x \equiv \text{NO} + \text{NO}_2$) affect air quality and human health directly by
46 contributing to premature mortality (Burnett et al., 2004; Tao et al., 2012) and asthma for children
47 and adults (Anenberg et al., 2018), and indirectly by acting as precursors for tropospheric ozone
48 (O_3) formation (Jacob et al., 1996), and nitrate aerosols (Bauer et al., 2007). Significant gaps in
49 ground-based monitoring of surface NO_2 concentrations and pronounced NO_2 heterogeneity
50 inhibit exposure assessment. To fill in knowledge of NO_2 exposures across a greater fraction of
51 the human population, satellite remote sensing offers the potential for spatially comprehensive
52 measurements. Major advances in satellite remote sensing from sun-synchronous low earth orbit
53 (LEO) have achieved global characterization of tropospheric NO_2 columns at specific times of the
54 day (Duncan et al., 2013; Veefkind et al., 2012) that have been applied to infer ground level NO_2
55 concentrations (Anenberg et al., 2022; Lamsal et al., 2011; Geddes and Martin, 2017; Cooper et
56 al., 2022). The emerging geostationary constellation (Al-Saadi et al., 2017) including the
57 Geostationary Environmental Monitoring Spectrophotometer (GEMS) over Asia, Tropospheric
58 Emissions: Monitoring Pollution (TEMPO) over North America, and Sentinel-4 over Europe
59 offers the prospect of inferring spatially comprehensive maps of hourly ground-level NO_2
60 concentrations. Towards this goal, there is need to develop an accurate representation of the hourly
61 NO_2 column to surface relationship.

62 Understanding the hourly variation of the relationship of NO_2 columns with surface
63 concentrations is of particular interest due to its role in the inference of hourly surface NO_2 from
64 satellite remote sensing. Numerous studies have separately examined the role of processes such as
65 surface emissions, boundary layer mixing, chemistry, deposition, and advection (Yang et al.,
66 2023b; Herman et al., 2009; Ghude et al., 2020; Zhang et al., 2016) upon the hourly variation of
67 NO_2 columns and upon surface NO_2 concentrations in the United States (Day et al., 2009), Spain



68 (Van Stratum et al., 2012), India (David and Nair, 2011), South Korea (Yang et al., 2023b, a) and
69 China (Tong et al., 2017). Differences have been identified in the daytime hourly variation of NO₂
70 tropospheric columns and surface concentrations during the DISCOVER-AQ and KORUS-AQ
71 campaigns with pronounced variation in surface concentrations that is not evident in the columns
72 (Choi et al., 2020; Crawford et al., 2021). Differences have also been noted in hourly variation of
73 NO₂ measured by aircraft and ground-based Pandora instruments (Li et al., 2021). There is a need
74 to understand the factors that can affect the relationship of hourly NO₂ columns with surface
75 concentrations.

76 Major challenges in the interpretation of satellite NO₂ observations include the short
77 lifetime of NO_x (Laughner and Cohen, 2019), and localized emissions (Crippa et al., 2018) that
78 affect its spatial heterogeneity. Coarse resolution inputs to satellite retrieval algorithms (e.g.,
79 terrain height, albedo, and a priori NO₂ profiles) can lead to biases (Laughner et al., 2019;
80 Laughner et al., 2018; Russell et al., 2011). Complications with ground-based measurements of
81 the NO₂ columns as part of Pandora include uncertainties at steeper solar zenith angles during
82 morning and evening hours (Herman et al., 2009; Reed et al., 2015) and the changing Pandora
83 field of view (FOV) during morning and late evening (Li et al., 2021). Non-linearities in the
84 relationship between NO₂ concentrations and NO_x sources or sinks can lead to biases in coarse-
85 resolution CTMs (Valin et al., 2011) that necessitate chemical transport models with a finer
86 resolution (Li et al., 2021, 2023a). Recent advances in the simulation of global atmospheric
87 composition at fine resolution (Eastham et al., 2018; Hu et al., 2018; Martin et al., 2022) offer the
88 opportunity to address the resolution need at the global scales of the geostationary constellation.

89 An important consideration in the inference of surface NO₂ concentrations with columnar



90 satellite observations is the vertical profile of NO₂ concentrations. Aircraft observations from the
91 NASA Deriving Information on Surface Conditions from Column and Vertically Resolved
92 Observations Relevant to Air Quality (DISCOVER-AQ) campaign offer measurements of the NO₂
93 vertical profile in the lower troposphere for evaluation of modeled vertical profiles (Flynn et al.,
94 2014; Reed et al., 2015). The Pandora Global Network (PGN) is a global sun photometer network
95 that offers hourly measurements of total NO₂ columns (Verhoelst et al., 2021), useful for
96 interpretation of the daytime variation of NO₂ columns and evaluation of simulated columns. In
97 this study, we use the summertime NO₂ measurements from the NASA P-3B aircraft and Pandora
98 sun photometers over Maryland, Texas, and Colorado during the DISCOVER-AQ campaign to
99 understand the hourly variation of the NO₂ vertical distribution. We sample the high-performance
100 GEOS-Chem (GCHP) simulations along aircraft flight tracks and account for line-of-sight of the
101 Pandora sun photometers to interpret the hourly variation of NO₂ vertical distribution and vertical
102 columns. We explore the effect of hourly variation of temperature on the NO₂ cross-section, and
103 the Pandora columns. We further investigate the hourly variation of NO₂ columns and surface
104 concentrations from 50 PGN sites across the northern hemisphere. Section 2 describes the datasets
105 and methods used in this study to interpret the variation of NO₂ columns, surface concentrations,
106 and vertical distribution over DISCOVER-AQ and PGN sites. Section 3 examines the consistency
107 between the NO₂ vertical columns and surface concentrations across DISCOVER-AQ sites, and
108 PGN sites across the CONUS, Europe, and Asia. We explore the effects of model resolution and
109 boundary layer height adjustments on the hourly variation of NO₂ total columns and surface
110 concentrations as a function of hourly variation in mixed layer depth and photochemistry, and
111 measurement characteristics of Pandora sun photometers over PGN sites across the CONUS,
112 Europe, and Asia.



113 **2 Materials and Methods**

114 **2.1 Aircraft measurements of NO₂ vertical profiles**

115 The DISCOVER-AQ campaign offers comprehensive datasets of airborne and surface
116 observations relevant for accessing air quality. One of the main objectives of the campaign was to
117 examine the hourly variation of the relationship between the column and surface concentrations.
118 In this study, we use aircraft, Pandora, and surface measurements over Maryland (July 2011),
119 Texas (September 2013) and Colorado (July-August 2014) to investigate the hourly variation of
120 NO₂ vertical profiles during summer when a long duration of daylight exists for analysis. Figure
121 A1 shows the flight tracks, altitude variation, roadways and Pandora instrument locations over
122 Maryland, Texas, and Colorado during the DISCOVER-AQ campaign. We focus on the aircraft
123 spirals since they are designed to sample the vertical profile. We use NO₂ concentrations measured
124 by the thermal dissociation laser-induced fluorescence (TD-LIF) technique (Thornton et al., 2000;
125 Day et al., 2002) during the campaign. The laser-induced fluorescence method is highly sensitive
126 for directly measuring NO₂, with a measurement uncertainty of 5 % and a detection limit of 30
127 pptv (Thornton et al., 2000). It also attempts to correct for positive interferences (Nault et al., 2015;
128 Yang et al., 2023b). We use aircraft measurements from a height of about 300 m above ground
129 level (AGL) up to 4 km AGL where high measurement frequency facilitates regional
130 representation.

131 **2.2 Pandonia Global Network NO₂ Total Column Densities**

132 PGN is a global network of ground-based sun photometers that measures sun and sky
133 radiance from 270 to 530 nm that allow retrievals of various trace gases including NO₂. Retrieval
134 precision for total vertical NO₂ columns (“NO₂ columns” hereafter) is 5.4×10^{14} molecules/cm²
135 with a nominal accuracy of 2.7×10^{15} molecules/cm² under clear-sky conditions (Herman et al.,



136 2009; Cede 2021). We use the level 2 data product from the version rnvs3p1-8 for PGN and for
137 DISCOVER-AQ the data available from <https://asdc.larc.nasa.gov/data/DISCOVER-AQ/>. We
138 also include surface NO₂ observations from co-located DISCOVER-AQ and PGN sites. We use
139 NO₂ columns and surface concentrations employed during the DISCOVER-AQ campaign from
140 18 sites over Maryland, Texas and Colorado. We also include NO₂ columns and surface
141 concentrations from 50 PGN sites (the US: 31, Europe: 10, Asia: 9) for June-July-August (JJA)
142 2019. We focus on the NO₂ observations between 9 AM - 6 PM local solar time, for consistency
143 in observation frequency across all PGN sites. Tables A1 and A2 contain the names and location
144 of the DISCOVER-AQ and PGN sites respectively. We exclude Pandora measurements with
145 SZA>80°. We use total NO₂ columns including the stratosphere because the use of external
146 information sources to remove the stratospheric NO₂ columns from PGN can introduce errors in
147 the residual tropospheric columns (Choi et al., 2020).

148 **2.3 GEOS-Chem simulations**

149 We use GCHP, the high-performance configuration of the GEOS-Chem model that
150 operates with a distributed-memory framework for massive parallelization (Eastham et al., 2018),
151 to interpret the NO₂ column, vertical distribution and surface observations. GCHP offers the ability
152 to simulate the entire atmospheric column needed to interpret Pandora measurements at a fine
153 spatial resolution needed to interpret aircraft measurements. GEOS-Chem is driven by assimilated
154 meteorological data from the NASA Goddard Earth Observation System (GEOS). GEOS-Chem
155 includes a comprehensive O_x-NO_x-VOC-halogen-aerosol chemical mechanism in the troposphere,
156 in addition to the unified tropospheric-stratospheric chemistry extension in the stratosphere
157 (Eastham et al., 2014). We use GEOS-Chem 14.1.1 which includes recent updates to GCHP
158 (Martin et al., 2022), NO_x heterogenous and cloud chemistry (Holmes et al., 2019), isoprene



159 chemistry (Bates and Jacob, 2019), and aromatic chemistry (Bates et al., 2021). The ISORROPIA
160 II module simulates the thermodynamic partitioning between the gas and condensed phase
161 (Fountoukis and Nenes, 2007). Natural emissions include biogenic VOCs (Weng et al., 2020),
162 lightning NO_x (Murray et al., 2012), and soil NO_x (Weng et al., 2020). GEOS-Chem includes an
163 updated aircraft NO_x emissions inventory for 2019, developed with the Aircraft Emissions
164 Inventory Code (Simone et al., 2013). Figure A2 shows the hourly variation of NO_x emissions
165 across the PGN sites. For interpretation of PGN measurements in 2019, we conduct the simulations
166 for the year 2019 using GEOS-FP meteorology and the stretched grid capability (Bindle et al.,
167 2021) at a cubed sphere resolution of C180 (~55 km) and stretch factor of 4.0 yielding a regional
168 refinement of ~12 km. All simulations were conducted with a two-week spin-up. We interpolate
169 hourly GCHP outputs of simulated NO₂ columns and surface concentrations to the local solar time
170 at the PGN observation sites.

171 For interpretation of the DISCOVER-AQ aircraft campaigns, we conduct stretched grid
172 simulations over Maryland (July 2011), Texas (September 2013) and Colorado (July-August 2014)
173 with identical stretched grid configurations, with sampling along the aircraft flight tracks. We use
174 MERRA-2 meteorology for these simulations as GEOS-FP meteorology datasets are not available
175 prior to 2014. A sensitivity test for the year 2019 using either GEOS-FP and MERRA-2 affects
176 the local simulated NO₂ columns and surface concentrations by less than 5% for both 12 km and
177 55 km resolutions.

178 Hourly variation of the planetary boundary layer height (PBLH) can influence the vertical
179 distribution and hence the surface concentration of aerosols and trace gases (Lin and McElroy,
180 2010). Millet et al., (2015) found that GEOS-FP reanalysis over-estimates daytime PBLH as
181 compared to observations; correcting for PBLH estimations can lead to better agreement of ozone



182 (Oak et al., 2019) and PM_{2.5} (Li et al., 2023b) with measurements. Our base case simulation uses
183 the PBLH derived from the Aircraft Meteorological Data Reports (AMDAR) at 54 sites across the
184 CONUS to adjust the PBLH estimates as described in Li et al., (2023). We examine the effect of
185 using the adjusted PBLH for simulations over the CONUS, Europe and East Asia. Table 1 shows
186 the 3 simulation cases conducted over Maryland, Texas, Colorado, the CONUS, Europe and East
187 Asia.

188 Table 1. Summary of GCHP Simulations

189	Name	Description
190	Base_12	12 km base
191	NoΔBL_12	12 km without PBLH modification
192	NoΔBL_55	55 km without PBLH modification

194 2.5 Effective temperature of Pandora measurements

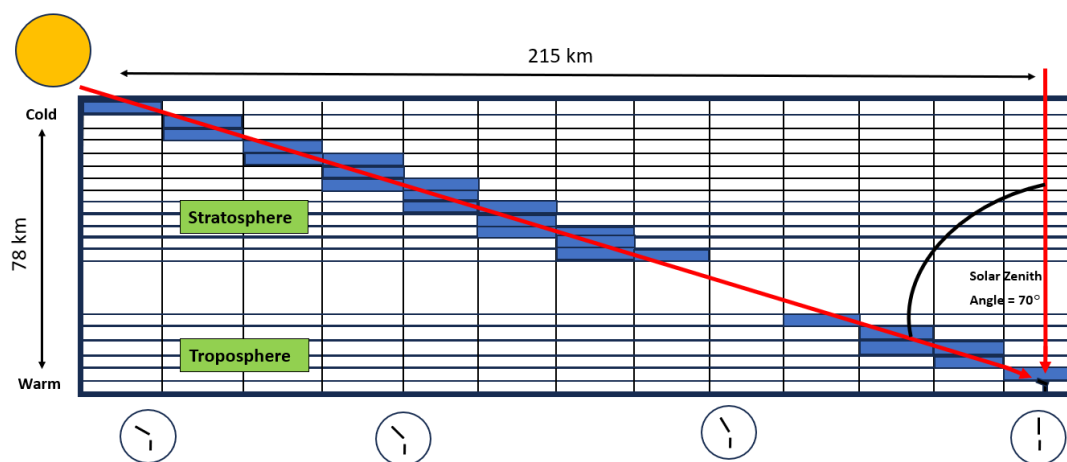
195 The NO₂ cross section is temperature dependent with the magnitude of spectral features in a 294
196 K NO₂ spectrum about 80% of those in 220 K NO₂ spectrum (Vandaele et al., 2002). Thus, the
197 NO₂ columns fitted with a 220 K NO₂ spectrum are about 80% of those fitted with the 294 K NO₂
198 spectrum. Prior studies have identifies biases in the Pandora total ozone column effective
199 temperature driven by variation in seasonal temperature (Zhao et al., 2016; Herman et al., 2015).
200 We compare Pandora NO₂ effective temperatures with for the site-specific vertical variation of
201 hourly effective temperature using hourly GEOS-FP temperature profiles and GCHP NO₂ vertical
202 profiles following equation (1) of Herman et al. (2009):

$$203 \quad T_{eff} = \frac{\sum_i^N (\sigma(NO_2)_i \cdot VC(NO_2)_i \cdot (T)_i)}{\sum_i^N (\sigma(NO_2)_i \cdot VC(NO_2)_i)} \quad (1)$$

204 2.6 Local solar time along Pandora line-of-sight



205 At observing scenarios with large solar zenith angles, the Pandora sun photometer observes air
 206 masses with varying local solar time at different altitudes along the line-of-sight. This feature is
 207 particularly noteworthy for comparing hourly Pandora observations with other measurements or
 208 simulations. Figure 1 shows the sampling process of GCHP simulations along the line-of-sight of
 209 the Pandora sun photometer GCHP grid boxes are integrated along the viewing geometry of the
 210 Pandora instrument to create a “staircase column” that accounts for effects of local solar time on
 211 the horizontal and vertical variation in NO₂ concentrations. The variation in local solar time is
 212 most relevant near sunrise and sunset when the NO₂/NO_x ratios changes rapidly as discussed in
 213 section 3.2. We correct the vertical columns reported by PGN to the local solar time of the
 214 instrument by applying the ratio of integrated staircase columns to vertical columns.



215

216 Figure 1. Configuration of integrating the GCHP grid boxes along the line-of-sight of the Pandora
 217 instrument. The shaded grid boxes represent the line-of-sight for the Pandora sun photometer at an inclined
 218 solar zenith angle. Clock faces indicate change in local solar time.

219 2.7 Ground based surface NO₂ measurements

220 We use hourly NO₂ surface concentrations from the catalytic converter measurements over
 221 DISCOVER-AQ and PGN sites. Based on the approach of Lamsal et al., (2008) and Shah et al.,

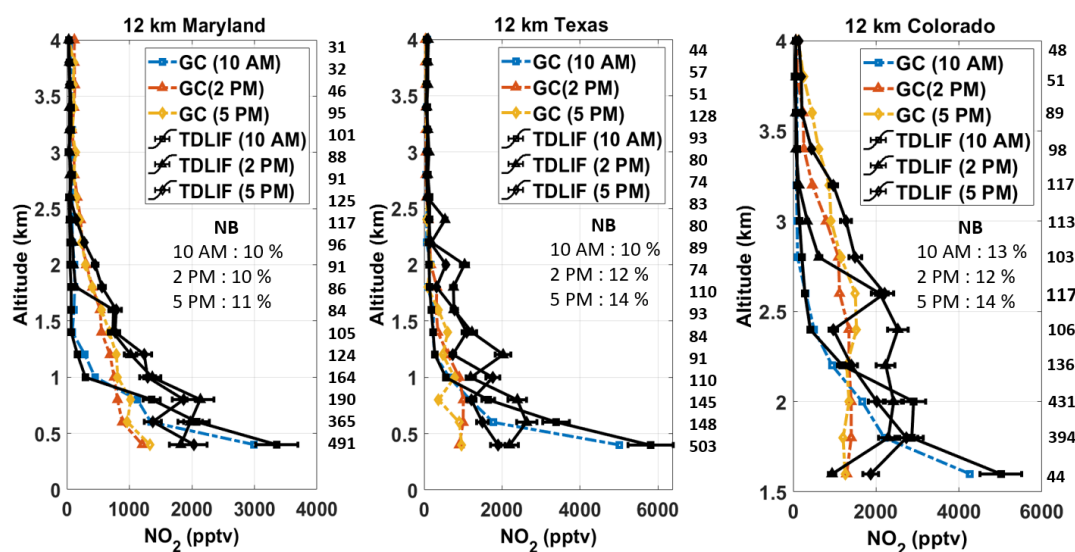


222 (2020), we correct the interference of organic nitrates and HNO₃ in the NO₂ measurements, using
 223 a correction factor derived from GCHP simulated site-specific NO₂, organic nitrates, and HNO₃
 224 mixing ratios. The correction for HNO₃ and organic nitrates reduced the summertime mean NO₂
 225 surface concentrations by 18% over DISCOVER-AQ sites and 23% over PGN sites.

226 3 Results and Discussion

227 3.1 Hourly variation of observed and simulated NO₂ vertical profiles

228 Figure 2 shows the hourly variation in the airborne TD-LIF measurements and simulated NO₂
 229 vertical profiles at 12 km resolution (Base_12) over Maryland, Texas and Colorado during the
 230 DISCOVER-AQ campaign. The measurements exhibit a pronounced maximum at 500 m at 10
 231 AM (squares) that diminishes by a factor of 2 in the afternoon as concentrations become more



232

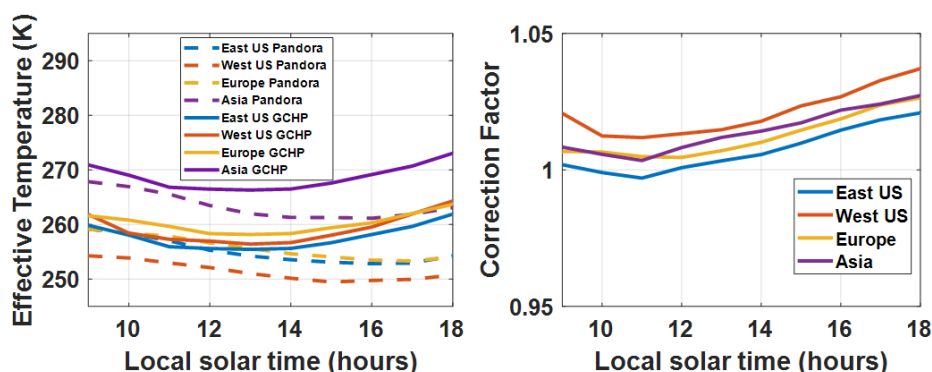
233 Figure 2: NO₂ vertical profiles from TD-LIF instrument aboard P-3B during the DISCOVER-AQ campaign
 234 over Maryland, Texas and Colorado. The black lines represent observations (square: 10 AM, triangle: 2
 235 PM, diamond: 5 PM). The colored lines represent 12 km GCHP simulated mixing ratios (blue: 10 AM,
 236 orange: 2 PM, yellow: 5 PM). The inset values in the boxes show the normalized biases (NBs) at 10 AM,
 237 2 PM, and 5 PM. The numbers on the right of each panel represent the number the observations associated
 238 with the corresponding altitude level. Error bars indicate standard errors in measurements.



239 uniform below 1.5 km (triangles and diamonds), driven by the hourly variation in PBLH mixing
 240 from early morning to late afternoon. For all three DISCOVER-AQ campaigns, the 12 km
 241 simulated NO₂ mixing ratios (left panel) represent the vertical profile well with normalized bias
 242 (NB) below 16% at local times: 10 AM, 2 PM, and 5 PM. The simulated NO₂ vertical profiles at
 243 12 km without PBLH modifications (NoABL_12) are similar (Figure A3). Figure A4 shows the
 244 55 km simulated NO₂ vertical profiles (NoABL_55). The 55 km GCHP simulations have increased
 245 NB by a factor of 2, as compared to at 12 km. Overall, the NO₂ vertical profile exhibits greater
 246 consistency with observations at 12 km than at 55 km by better resolving the heterogeneous
 247 conditions along the aircraft flight tracks.

248 3.2 Corrections to Pandora Effective Temperature

249 The left panel in Figure 3 shows the Pandora and simulated mean hourly effective temperature of
 250 the NO₂ columns over all PGN sites during June-August as inferred using hourly GEOS-FP



251

252 Figure 3. Hourly variation of the total NO₂ column mean effective temperature across all PGN sites (left
 253 panel) and the corresponding correction factors (right panel).

254 temperature profiles and GCHP NO₂ vertical profiles. The simulated effective temperature is
 255 lowest in early afternoon when near-surface NO₂ concentrations are minimum such that
 256 stratospheric NO₂ makes a larger fractional contribution to the total column. The simulated



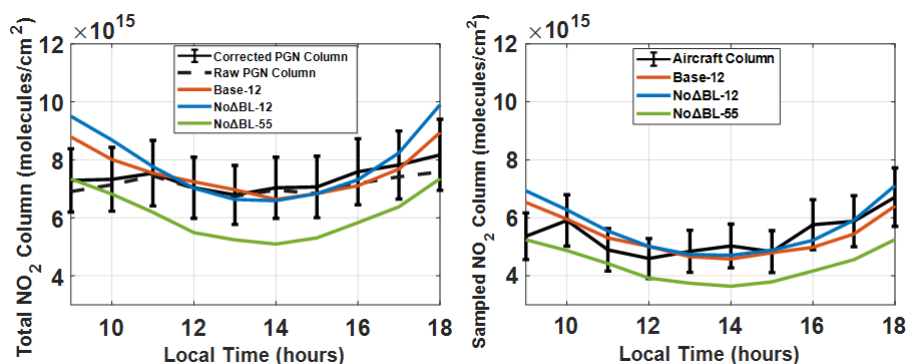
257 effective temperature deviates from the Pandora effective temperature with an increase toward
 258 sunrise and sunset with increasing near-surface NO₂ fraction. The corresponding correction factor
 259 (CF) for hourly variation in the effective temperature calculated as:

$$260 \quad CF = 1 + \frac{0.2(T_{eff}(GCHP(hour)) - T_{eff}(Pandora(hour)))}{294 - 220} \quad (2)$$

261 The CF for the Pandora NO₂ columns increases toward sunrise and sunset due to the increased
 262 effective temperature, reflecting the greater abundance of NO₂ molecules observed per unit
 263 absorption. We apply site-specific CFs across all Pandora observations.

264 3.3 Hourly variation of observed and simulated NO₂ VCDs

265 Figure 4 (left) shows the mean hourly daytime Pandora vertical NO₂ columns summarized
 266 from the summertime DISCOVER-AQ campaign measurements. The raw Pandora NO₂ columns



267
 268

269 Figure 4. The left panel shows the total NO₂ vertical columns from corrected Pandora columns (black), raw
 270 Pandora columns (black dotted), the 12 km base case simulation with staircase columns (red), 12 km without
 271 modified PBLH (blue) and 55 km without modified PBLH (green), during the DISCOVER-AQ campaigns
 272 over Maryland (2011), Texas (2013) and Colorado (2014). The corrected PGN columns account for the
 273 hourly variation in the effective temperature and the local solar time along the line-of-sight. The right panel
 274 shows sampled aircraft and simulated partial columns (300 m A.G.L - 4 km A.G.L). Error bars indicate
 275 standard error.

276

277 exhibit weak hourly variation of 8×10^{14} molecules cm⁻² (within 10% of the daytime mean) that

278 is inconsistent with the aircraft measurements that indicate total columns in the morning and

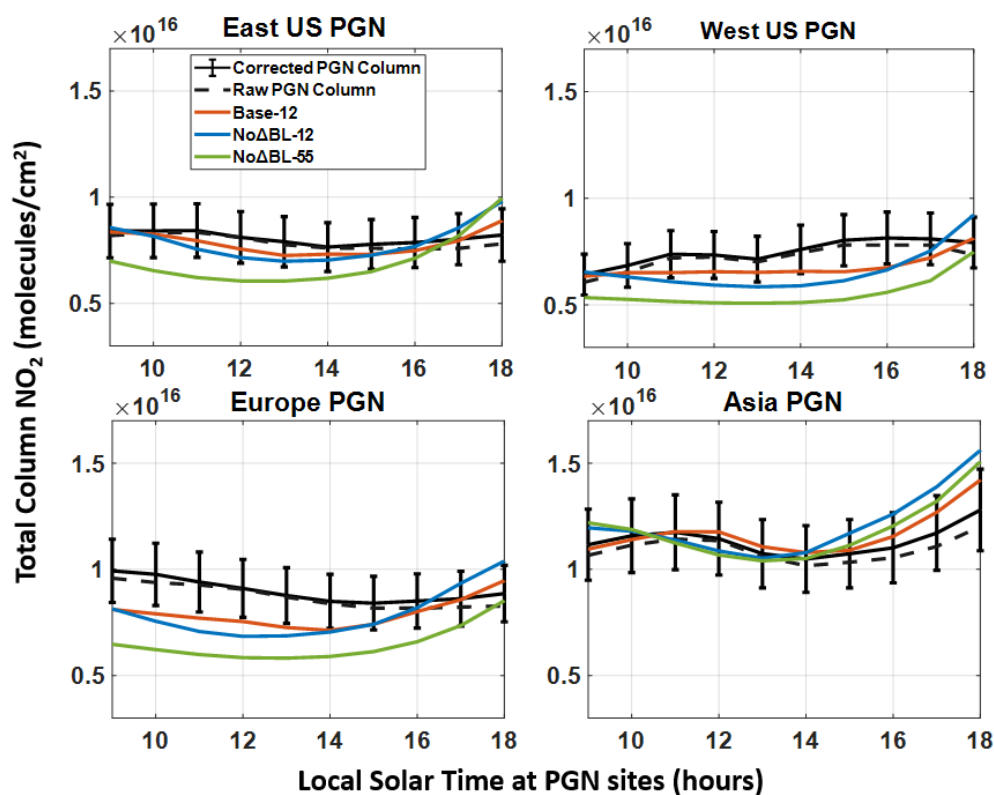


279 evening of about 1.5×10^{15} molecules cm^{-2} greater than afternoon. The corrected Pandora
280 measurements that account for hourly variation in effective temperature and local solar time along
281 line-of-sight exhibit greater NO_2 columns in morning and evening by about 1.3×10^{15} molecules
282 cm^{-2} , similar to the aircraft measurements. Since the Pandora instruments track the sun, viewing
283 stratospheric air masses 100 - 200 km away from the measurement station to the East in the
284 morning and to the West in the evening, the local solar time of stratospheric NO_2 observed by
285 Pandora instruments near sunrise and sunset is systematically shifted by about 5-10 mins towards
286 noon. This shift can be particularly important during sunrise and sunset when NO_2 columns in the
287 stratosphere undergo pronounced increase driven by an increasing NO_2/NO_x ratio (Figure A5).
288 The 12 km simulated vertical columns generally represent the corrected Pandora observed columns
289 with an NB of 10%. Excluding the PBLH modification would have increased the NB to 13%.
290 Using a coarser 55 km simulation would have further degraded the agreement with an NB of 19%.
291 The hourly variation of partial NO_2 columns over 300 m to 4 km AGL from aircraft observations
292 exhibits a distinct increase in morning and evening and are well represented by the 12 km base
293 case simulation (NB =13%). Similar to our analysis for Pandora sites, excluding the PBLH
294 modification and coarsening the simulation to 55 km degrades the performance (NB = 15% and
295 25%) versus aircraft columns.

296 Figure 5 extends our analysis to all PGN sites across the CONUS, Europe and East Asia. Raw
297 measurements across all regions exhibit weak hourly variation. The correction for effective
298 temperature and local solar time along Pandora line-of-site increases the mean NO_2 columns in the
299 morning and evening by about 6×10^{14} molecules cm^{-2} across all regions. The base case simulation
300 generally reproduces measurements with NB of 9% for the eastern US, 14% for western US, 15%
301 for the Europe and 21% for east Asia sites. Excluding the PBLH correction would have increased



302 the NB (eastern US: 12%, western US: 18%, Europe: 18%, and eastern Asia: 26%) with the largest
 303 change in Asia. Excluding the PBLH correction yields a higher daytime PBLH resulting in
 304 increased chemical lifetime of NO_x, reduced NO₂ dry deposition rates and increased NO₂/NO_x
 305 ratio during afternoon and evening (Figure A6), thus leading to an hourly variation that deviates



306

307 Figure 5. The total NO₂ vertical columns from corrected Pandora columns (black), raw Pandora columns
 308 (black dotted), the 12 km base case simulation with staircase columns (red), 12 km without modified PBLH
 309 (blue) and 55 km without modified PBLH (green) sampled over PGN sites for the summer months of June-
 310 July-August in 2019. Error bars indicate standard error.

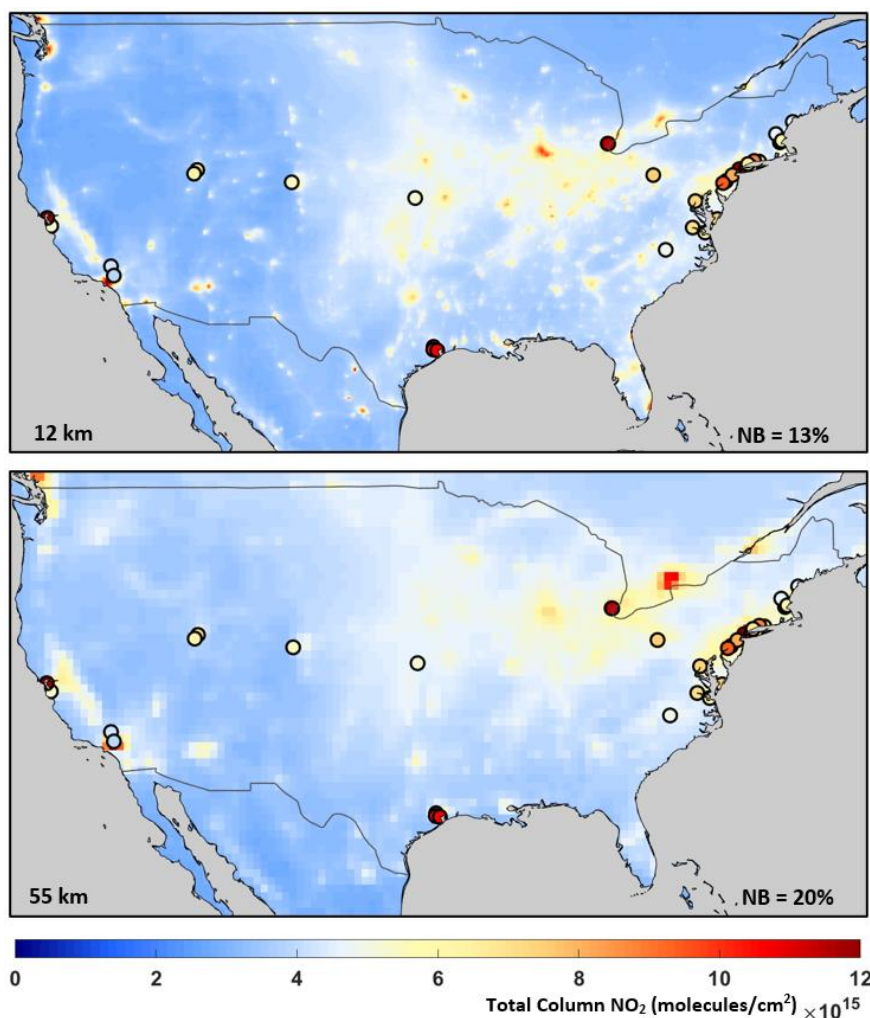
311 from the Pandora observations. Coarser resolution generally further increased the bias, reflecting
 312 resolution effects discussed in the next section. The increase of the simulated total NO₂ columns
 313 between 3-6 PM across all PGN sites reflects an increase in the NO₂/NO_x ratio throughout the
 314 column, driven by a reduction in HO_x (Figure A7).



315 **3.3 Simulated total NO₂ columns**

316 Figure 6 shows the 12 km and 55 km simulated total NO₂ columns, for the summer months of

317 June-July-August in 2019, between 9 AM and 6 PM (local solar time) over the CONUS. The



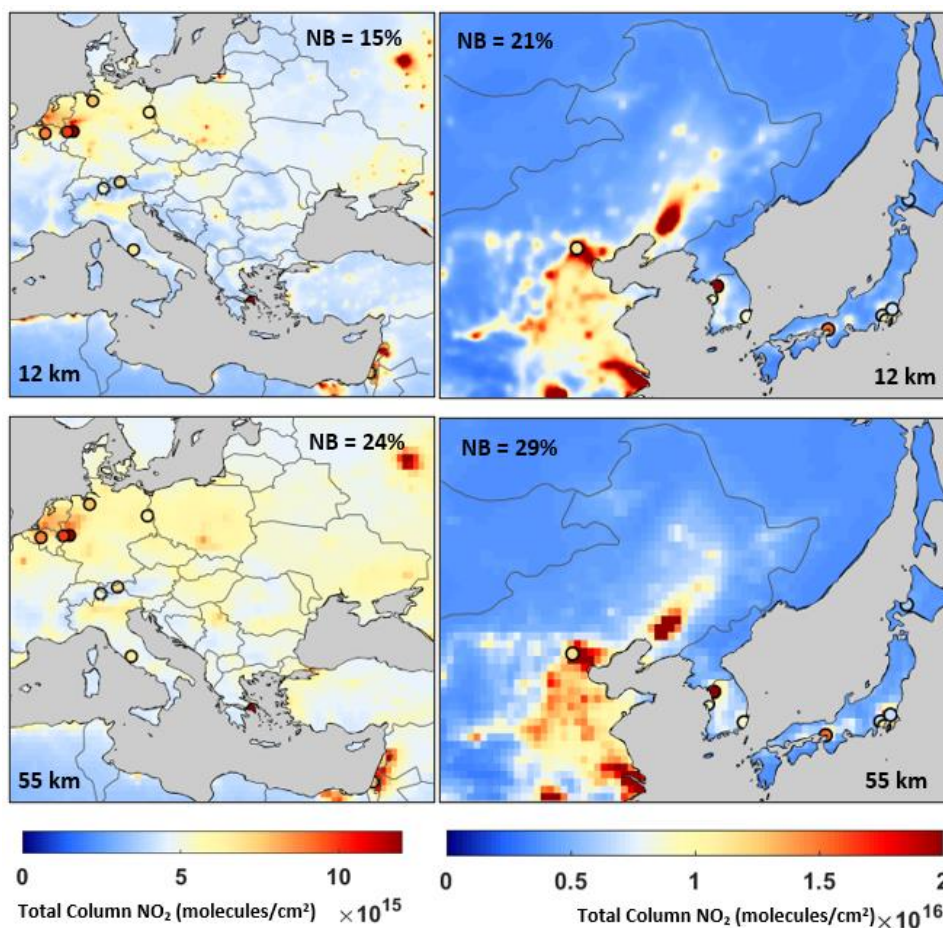
318

319 Figure 6. Simulated NO₂ total columns at 12 km (panel A) and 55 km (panel B) horizontal resolutions for
320 the three-month average of June-July-August 2019 over domains where PGN monitors were available
321 between 9 AM – 6 PM local solar time. The solid circles represent the PGN mean total columns between
322 9 AM – 6 PM local solar time for PGN sites in CONUS (31)

323 overlaid circles show the PGN mean total NO₂ columns. The 12 km simulated NO₂ columns



324 exhibit greater heterogeneity and better consistency with PGN observed columns (NB = 13%) as
325 compared to the 55 km simulated NO₂ columns (NB = 20%). This is primarily driven by better
326 representation of emission and chemical processes at fine resolution (Zhang et al., 2023; Li et al.,
327 2023a). Emissions at these sites are dominated by the transportation sector (Table A3). Figure 7
328 shows the total NO₂ columns from PGN, 12 km and 55 km for the summer months of June-July-



329

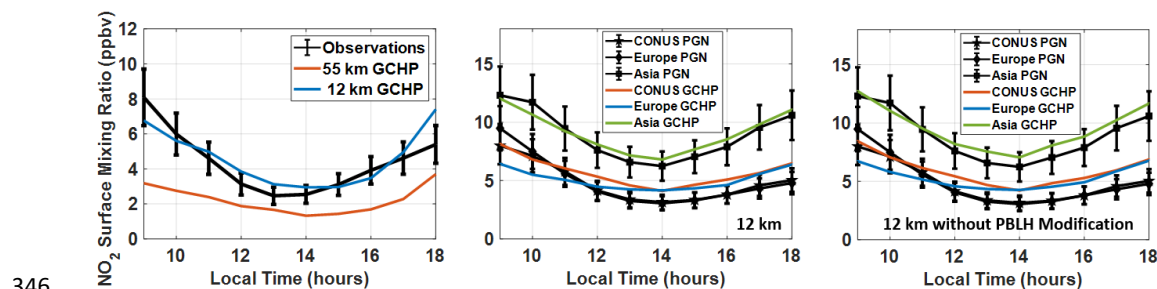
330 Figure 7. Simulated NO₂ total columns at 12 km (panel C and D) and 55 km (panel E and F) horizontal
331 resolutions for the three-month average of June-July-August 2019 over domains where PGN monitors were
332 available between 9 AM – 6 PM local solar time. The solid circles represent the PGN mean total columns
333 between 9 AM – 6 PM local solar time for the PGN sites in Europe (10) and Asia (9).



334 August in 2019, between 9 AM and 6 PM local solar time over Europe and East Asia. We find
 335 enhanced NO₂ vertical columns over urban areas in western Europe, eastern China, Japan and the
 336 Korean peninsula. The 12 km simulated NO₂ columns exhibit more resolved combustion features
 337 and better agreement with Pandora observed columns for Europe (NB = 15%) and east Asia (NB
 338 =17%) as compared to the 55 km simulated NO₂ columns for Europe (NB =24%) and east Asia
 339 (NB =29%).

340 3.4 Hourly variation of observed and simulated surface NO₂ concentrations

341 Figure 8 shows the hourly variation in surface NO₂ mixing ratios from the corrected in situ
 342 measurements and 12 km simulations over Maryland, Texas and Colorado. Measured NO₂ mixing
 343 ratios are greater in morning and evening than in afternoon as expected from the mixed layer
 344 growth and shorter NO_x lifetime in afternoon. Observed NO₂ surface concentrations over PGN
 345 sites in Asia show enhancement at evening hours (5-6 PM) as compared to PGN sites elsewhere.



347 Figure 8. The left panel shows the hourly variation of corrected surface NO₂ mixing ratios from
 348 observations during the DISCOVER-AQ campaign. The middle and right panels show the hourly variation
 349 of observed and 12 Km PBLH modified and 12 km simulated surface NO₂ mixing ratios averaged over the
 350 PGN sites respectively. Error bars indicate standard error.

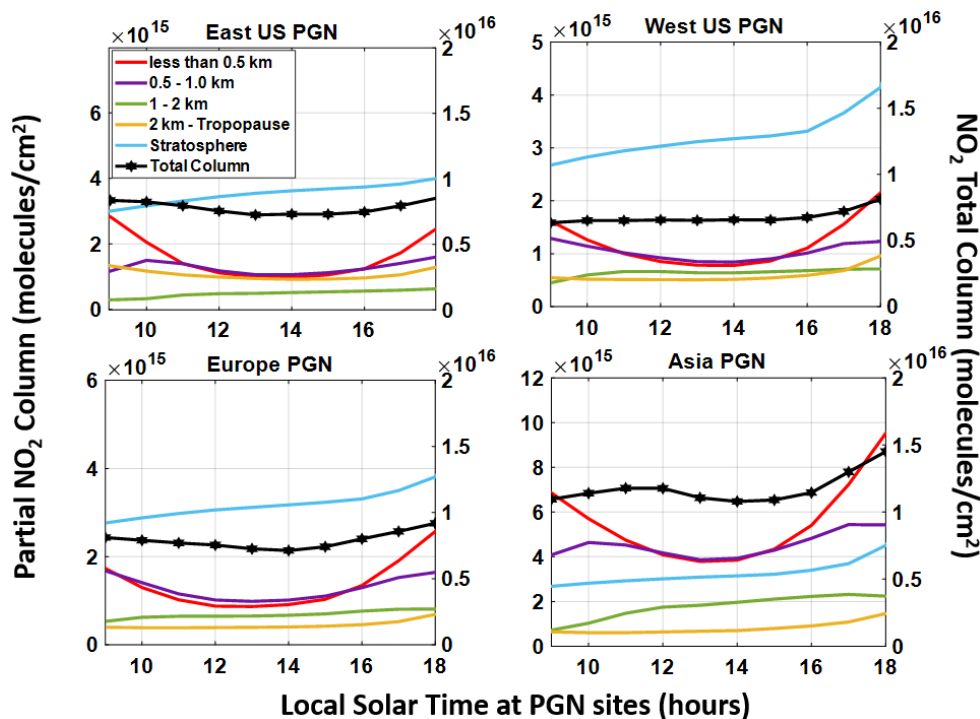
351 The measurements are better represented at 12 km (NB = 21%) than at 55 km (NB =63%) by better
 352 resolving high NO_x emissions near measurement sites. Both Base_12 and NoABL_12 simulated
 353 NO₂ concentrations generally represent the observations well with NB = 18% (Base_12) and NB



354 = 20% (No Δ BL₁₂), across all PGN sites.

355 3.5 Hourly variation of layer contributions to total NO₂ staircase columns

356 We proceed to apply the 12 km simulations to understand how the NO₂ vertical profile affects the
 357 NO₂ column to surface relationship. Figure 9 shows the hourly variation of simulated contributions
 358 to the NO₂ total columns (Base₁₂) from different vertical layers for multiple regions. In all four
 359 regions, within the troposphere, the layer below 0.5 km is the largest contributor at 9 AM with a
 360 diminishing contribution into the afternoon associated with mixed layer growth and an increasing
 361 contribution towards evening. The contribution from layers between 0.5 km and the tropopause



362

363 Figure 9. The simulated absolute contribution of NO₂ columns at different hours of the day averaged over
 364 the summer months of June-July-August for 2019 for PGN sites over the eastern US, western US, Europe,
 365 and eastern Asia. The colored lines resemble the absolute concentrations from different sections of the
 366 column. The black line (hexagon) represents the total NO₂ column. The right y-axis (specifically for the
 367 total NO₂ column representing the black marked line) shows the total columns of NO₂.



368 has weaker variation contributing to the overall weaker variation in total columns. Fractional layer
369 contributions are shown in Figure A8. Fractional hourly variation of the layers above 0.5 km
370 exhibits a compensating inverse behavior, with a pronounced variation in the stratospheric
371 fraction. Contributions from the free troposphere are relatively high for the eastern US reflecting
372 the lightning contribution (Shah et al., 2023; Dang et al., 2023). Over Asia the fractional
373 contribution below 0.5 km is the highest (26% - 42%) reflecting major surface contributions.
374 Overall, we find that for all four regions, the hourly variation in the total column reflects hourly
375 variation below 500 m, dampened by greater column contributions above 500 m that dominate the
376 total column.

377 **Conclusion**

378 We applied the GCHP model to investigate the hourly variation of summertime NO₂ columns and
379 surface concentrations by interpreting DISCOVER-AQ aircraft and ground-based measurements
380 over Maryland, Texas, Colorado and PGN measurements over the CONUS, Europe, and eastern
381 Asia. We corrected the hourly variation in Pandora observations for the effects of temperature on
382 the NO₂ cross section and the local solar time along the Pandora line-of-sight. The site-specific
383 effective temperature correction factors typically increase the hourly variation of the Pandora
384 observed columns over DISCOVER_AQ sites (3.5% from the daytime mean) and PGN sites (4%
385 from the daytime mean). Near sunrise and sunset, differences in local solar time observed by
386 Pandora in the stratosphere versus the measurement site reflect displacement of 5-10 mins in local
387 solar time toward noon which is relevant in the stratosphere near sunrise and sunset when the
388 NO₂/NO_x ratio is varying rapidly. These corrections to the Pandora measurements improve their
389 consistency with the hourly variation in the NO₂ columns inferred from DISCOVER-AQ aircraft
390 measurements. We find that the fine scale simulations at 12 km better represent the NO₂ vertical



391 profile measured by aircraft, reducing the NB from 23% to 16% as compared to the simulations at
392 moderate resolution of 55 km. Simulations at fine resolution (~12 km) of vertical columns along
393 the line-of-sight of Pandora instruments agree better with Pandora sun photometers at
394 DISCOVER-AQ sites (10%), and across the eastern US (9%), western US (14%), Europe (15%)
395 and Asia (21%) as compared to moderate resolution (55 km). Fine resolution represents
396 atmospheric physical and chemical processes with greater accuracy. Excluding the effects of
397 model resolution, and the PBLH modification increases the NB to 21% across DISCOVER-AQ
398 sites (over Maryland, Texas and Colorado) and increases the NB at PGN sites over the eastern US
399 (17%), western US (24%) , Europe (24%) and east Asia (29%). Adjusting the PBLH to represent
400 observations improved the daytime variation in NO_2/NO_x ratios by increasing the NO_2/NO_x ratio
401 in midday and decreasing the NO_2/NO_x ratio in afternoon and evening.

402 We use the simulated columns to derive the hourly contribution of vertical layers to the
403 total tropospheric columns. We find weaker hourly variation in NO_2 columns than in the lowest
404 500 m where NO_2 concentrations are greater in morning and evening than midday, while the
405 residual tropospheric column above 500 m dominates the total column with weaker variability.
406 Thus, the weak hourly variation in the column reflects fractional contributions from NO_2 below
407 and above 500 m. Future work should leverage the information developed here to test the
408 performance of surface NO_2 concentrations inferred from the geostationary constellation versus
409 ground-based measurements.

410 **Code and Data Availability**

411 GEOS-Chem 14.1.1 along with GCHP code is available for download at
412 <https://github.com/geoschem/GCHP.git>. The PGN data is available at [https://data.pandonia-](https://data.pandonia-global-network.org/)
413 [global-network.org/](https://data.pandonia-global-network.org/). The DISCOVER-AQ aircraft and Pandora data are available here:



414 <https://asdc.larc.nasa.gov/project/DISCOVER-AQ>. For hourly simulated NO₂ datasets please
415 contact the author (deepangsuchatterjee@wustl.edu; deepangsuchatterjee@gmail.com)

416 **Author contributions**

417 The manuscript was written using contributions from all authors. The conceptualization was
418 initialized by DC and RVM. The methodology was developed by DC and RVM .DC conducted
419 the model simulations. DC conducted the data analysis with help from CL,DZ,HZ,LL,DH,RC. JC
420 conducted the DISCOVER-AQ campaign. AC manages the PGN datasets. DC and RVM wrote
421 the original draft. All authors have reviewed, edited and given approval to the final version of the
422 manuscript.

423 **Competing interests**

424 The contact author has declared that neither they nor their co-authors have any competing interests.

425

426 **Acknowledgments**

427 This work has been supported by the NASA Grant 80NSSC21K1343 and 80NSSC21K0508 and
428 NSF Grant 2244984. We thank the GEOS-Chem support team for maintaining the model used in
429 this work.

430 **Reference**

- 431 Al-Saadi, J., Kim, J., Lambert, J.-C., Veihelmann, B., and Chance, K.: Geostationary Satellite
432 Constellation for Observing Global Air Quality : Geophysical Validation Needs, 2017.
- 433 Anenberg, S. C., Henze, D. K., Tinney, V., Kinney, P. L., Raich, W., Fann, N., Malley, C. S., Roman, H.,
434 Lamsal, L., Duncan, B., Martin, R. V., van Donkelaar, A., Brauer, M., Doherty, R., Jonson, J. E., Davila,
435 Y., Sudo, K., and Kuylentierna, J. C. I.: Estimates of the global burden of ambient PM_{2.5}, ozone, and
436 NO₂ on asthma incidence and emergency room visits, *Environ. Health Perspect.*, 126, 1–14,
437 <https://doi.org/10.1289/EHP3766>, 2018.
- 438 Anenberg, S. C., Mohegh, A., Goldberg, D. L., Kerr, G. H., Brauer, M., Burkart, K., Hystad, P., Larkin,
439 A., Wozniak, S., and Lamsal, L.: Long-term trends in urban NO₂ concentrations and associated paediatric
440 asthma incidence: estimates from global datasets, *Lancet Planet. Heal.*, 6, e49–e58,



- 441 [https://doi.org/10.1016/S2542-5196\(21\)00255-2](https://doi.org/10.1016/S2542-5196(21)00255-2), 2022.
- 442 Bates, K. H. and Jacob, D. J.: A new model mechanism for atmospheric oxidation of isoprene: Global
443 effects on oxidants, nitrogen oxides, organic products, and secondary organic aerosol, *Atmos. Chem.*
444 *Phys.*, 19, 9613–9640, <https://doi.org/10.5194/acp-19-9613-2019>, 2019.
- 445 Bates, K. H., Jacob, D. J., Li, K., Ivatt, P. D., Evans, M. J., Yan, Y., and Lin, J.: Development and
446 evaluation of a new compact mechanism for aromatic oxidation in atmospheric models, *Atmos. Chem.*
447 *Phys.*, 21, 18351–18374, <https://doi.org/10.5194/acp-21-18351-2021>, 2021.
- 448 Bauer, S. E., Koch, D., Unger, N., Metzger, S. M., Shindell, D. T., and Streets, D. G.: Nitrate aerosols
449 today and in 2030: A global simulation including aerosols and tropospheric ozone, *Atmos. Chem. Phys.*,
450 7, 5043–5059, <https://doi.org/10.5194/acp-7-5043-2007>, 2007.
- 451 Belinha, J.: Manual for FEMAS Manual for FEMAS, 1–83, 2016.
- 452 Bindle, L., Martin, R. V., Cooper, M. J., Lundgren, E. W., Eastham, S. D., Auer, B. M., Clune, T. L.,
453 Weng, H., Lin, J., Murray, L. T., Meng, J., Keller, C. A., Putman, W. M., Pawson, S., and Jacob, D. J.:
454 Grid-stretching capability for the GEOS-Chem 13.0.0 atmospheric chemistry model, *Geosci. Model Dev.*,
455 14, 5977–5997, <https://doi.org/10.5194/GMD-14-5977-2021>, 2021.
- 456 Burnett, R. T., Stieb, D., Brook, J. R., Cakmak, S., Dales, R., Raizenne, M., Vincent, R., and Dann, T.:
457 Associations between Short-Term Changes in Nitrogen Dioxide and Mortality in Canadian Cities, *Arch.*
458 *Environ. Heal. An Int. J.*, 59, 228–236, <https://doi.org/10.3200/AEOH.59.5.228-236>, 2004.
- 459 Cede (2021) [https://www.pandonia-global-](https://www.pandonia-global-network.org/wpcontent/uploads/2021/09/BlickSoftwareSuite_Manual_v1-8-4.pdf)
460 [network.org/wpcontent/uploads/2021/09/BlickSoftwareSuite_Manual_v1-8-4.pdf](https://www.pandonia-global-network.org/wpcontent/uploads/2021/09/BlickSoftwareSuite_Manual_v1-8-4.pdf)
- 461 Choi, S., Lamsal, L. N., Follette-Cook, M., Joiner, J., Krotkov, N. A., Swartz, W. H., Pickering, K. E.,
462 Loughner, C. P., Appel, W., Pfister, G., Saide, P. E., Cohen, R. C., Weinheimer, A. J., and Herman, J. R.:
463 Assessment of NO₂ observations during DISCOVER-AQ and KORUS-AQ field campaigns, *Atmos.*
464 *Meas. Tech.*, 13, 2523–2546, <https://doi.org/10.5194/amt-13-2523-2020>, 2020.
- 465 Cooper, M. J., Martin, R. V., Hammer, M. S., Levelt, P. F., Veeffkind, P., Lamsal, L. N., Krotkov, N. A.,
466 Brook, J. R., and McLinden, C. A.: Global fine-scale changes in ambient NO₂ during COVID-19
467 lockdowns, *Nature*, 601, 380–387, <https://doi.org/10.1038/s41586-021-04229-0>, 2022.
- 468 Crawford, J. H., Ahn, J., Al-saadi, J., Chang, L., Emmons, L. K., Kim, J., Lee, G., Park, J., Park, R. J.,
469 Woo, J. H., Song, C., Hong, J., Hong, Y., Lefer, B. L., Lee, M., Lee, T., Kim, S., Min, K., Yum, S. S.,
470 Shin, H. J., Kim, Y., Choi, J., Park, J., Szykman, J. J., Long, R. W., Jordan, C. E., Simpson, I. J., Fried,
471 A., Dibb, J. E., Cho, S., and Kim, Y. P.: The Korea-United States Air Quality (KORUS-AQ) field study,
472 1–27, 2021.
- 473 Crippa, M., Guizzardi, D., Muntean, M., Schaaf, E., Dentener, F., Van Aardenne, J. A., Monni, S.,
474 Doering, U., Olivier, J. G. J., Pagliari, V., and Janssens-Maenhout, G.: Gridded emissions of air pollutants
475 for the period 1970-2012 within EDGAR v4.3.2, *Earth Syst. Sci. Data*, 10, 1987–2013,
476 <https://doi.org/10.5194/essd-10-1987-2018>, 2018.
- 477 Dang, R., Jacob, D. J., Shah, V., Eastham, S. D., Fritz, T. M., Mickley, L. J., Liu, T., Wang, Y., and
478 Wang, J.: Background nitrogen dioxide (NO₂) over the United States and its implications for satellite
479 observations and trends: effects of nitrate photolysis, aircraft, and open fires, *Atmos. Chem. Phys.*, 23,
480 6271–6284, <https://doi.org/10.5194/acp-23-6271-2023>, 2023.
- 481 David, L. M. and Nair, P. R.: Diurnal and seasonal variability of surface ozone and NO_x at a tropical
482 coastal site: Association with mesoscale and synoptic meteorological conditions, *J. Geophys. Res.*, 116,
483 1–16, <https://doi.org/10.1029/2010jd015076>, 2011.



- 484 Day, D. A., Wooldridge, P. J., Dillon, M. B., Thornton, J. A., and Cohen, R. C.: A thermal dissociation
485 laser-induced fluorescence instrument for in situ detection NO₂, peroxy nitrates, alkyl nitrates, and
486 HNO₃, *J. Geophys. Res. Atmos.*, 107, <https://doi.org/10.1029/2001jd000779>, 2002.
- 487 Day, D. A., Farmer, D. K., Goldstein, A. H., Wooldridge, P. J., Minejima, C., and Cohen, R. C.:
488 Observations of NO_x, opNs, σaNs, and HNO₃ at a rural site in the California Sierra Nevada Mountains:
489 Summertime diurnal cycles, *Atmos. Chem. Phys.*, 9, 4879–4896, [https://doi.org/10.5194/acp-9-4879-](https://doi.org/10.5194/acp-9-4879-2009)
490 2009, 2009.
- 491 Duncan, B. N., Yoshida, Y., De Foy, B., Lamsal, L. N., Streets, D. G., Lu, Z., Pickering, K. E., and
492 Krotkov, N. A.: The observed response of Ozone Monitoring Instrument (OMI) NO₂ columns to NO_x
493 emission controls on power plants in the United States: 2005–2011, *Atmos. Environ.*, 81, 102–111,
494 <https://doi.org/10.1016/j.atmosenv.2013.08.068>, 2013.
- 495 Eastham, S. D., Weisenstein, D. K., and Barrett, S. R. H.: Development and evaluation of the unified
496 tropospheric-stratospheric chemistry extension (UCX) for the global chemistry-transport model GEOS-
497 Chem, *Atmos. Environ.*, 89, 52–63, <https://doi.org/10.1016/j.atmosenv.2014.02.001>, 2014.
- 498 Eastham, S. D., Long, M. S., Keller, C. A., Lundgren, E., Yantosca, R. M., Zhuang, J., Li, C., Lee, C. J.,
499 Yannetti, M., Auer, B. M., Clune, T. L., Kouatchou, J., Putman, W. M., Thompson, M. A., Trayanov, A.
500 L., Molod, A. M., Martin, R. V., and Jacob, D. J.: GEOS-Chem high performance (GCHP v11-02c): A
501 next-generation implementation of the GEOS-Chem chemical transport model for massively parallel
502 applications, *Geosci. Model Dev.*, 11, 2941–2953, <https://doi.org/10.5194/GMD-11-2941-2018>, 2018.
- 503 Flynn, C. M., Pickering, K. E., Crawford, J. H., Lamsal, L., Krotkov, N., Herman, J., Weinheimer, A.,
504 Chen, G., Liu, X., Szykman, J., Tsay, S. C., Loughner, C., Hains, J., Lee, P., Dickerson, R. R., Stehr, J.
505 W., and Brent, L.: Relationship between column-density and surface mixing ratio: Statistical analysis of
506 O₃ and NO₂ data from the July 2011 Maryland DISCOVER-AQ mission, *Atmos. Environ.*, 92, 429–441,
507 <https://doi.org/10.1016/j.atmosenv.2014.04.041>, 2014.
- 508 Fountoukis, C. and Nenes, A.: ISORROPIAII: A computationally efficient thermodynamic equilibrium
509 model for K⁺-Ca²⁺-Mg²⁺-NH₄⁺-Na⁺-SO₄²⁻-NO₃⁻-Cl⁻-H₂O aerosols, *Atmos. Chem. Phys.*, 7, 4639–
510 4659, <https://doi.org/10.5194/ACP-7-4639-2007>, 2007.
- 511 Geddes, J. A. and Martin, R. V.: Global deposition of total reactive nitrogen oxides from, *Atmos. Chem.*
512 *Phys.*, 17, 10071–10091, 2017.
- 513 Ghude, S. D., Karumuri, R. K., Jena, C., Kulkarni, R., Pfister, G. G., Sajjan, V. S., Pithani, P., Debnath,
514 S., Kumar, R., Upendra, B., Kulkarni, S. H., Lal, D. M., Vander A, R. J., and Mahajan, A. S.: What is
515 driving the diurnal variation in tropospheric NO₂ columns over a cluster of high emission thermal power
516 plants in India?, *Atmos. Environ. X*, 5, 100058, <https://doi.org/10.1016/j.aeaoa.2019.100058>, 2020.
- 517 Herman, J., Cede, A., Spinei, E., Mount, G., Tzortziou, M., and Abuhassan, N.: NO₂ column amounts
518 from ground-based Pandora and MFDOAS spectrometers using the direct-sun DOAS technique:
519 Intercomparisons and application to OMI validation, *J. Geophys. Res. Atmos.*, 114, 1–20,
520 <https://doi.org/10.1029/2009jd011848>, 2009.
- 521 Herman, J., Evans, R., Cede, A., Abuhassan, N., Petropavlovskikh, I., and McConville, G.: Comparison
522 of ozone retrievals from the Pandora spectrometer system and Dobson spectrophotometer in Boulder,
523 Colorado, *Atmos. Meas. Tech.*, 8, 3407–3418, <https://doi.org/10.5194/amt-8-3407-2015>, 2015.
- 524 Holmes, C. D., Bertram, T. H., Confer, K. L., Graham, K. A., Ronan, A. C., Wirks, C. K., and Shah, V.:
525 The Role of Clouds in the Tropospheric NO_x Cycle: A New Modeling Approach for Cloud Chemistry
526 and Its Global Implications, *Geophys. Res. Lett.*, 46, 4980–4990, <https://doi.org/10.1029/2019GL081990>,
527 2019.



- 528 Hu, L., Keller, C. A., Long, M. S., Sherwen, T., Auer, B., Da Silva, A., Nielsen, J. E., Pawson, S.,
529 Thompson, M. A., Trayanov, A. L., Travis, K. R., Grange, S. K., Evans, M. J., and Jacob, D. J.: Global
530 simulation of tropospheric chemistry at 12.5 km resolution: Performance and evaluation of the GEOS-
531 Chem chemical module (v10-1) within the NASA GEOS Earth system model (GEOS-5 ESM), *Geosci.*
532 *Model Dev.*, 11, 4603–4620, <https://doi.org/10.5194/gmd-11-4603-2018>, 2018.
- 533 Jacob, D. J., Heikes, B. G., Fan, S. M., Logan, J. A., Mauzerall, D. L., Bradshaw, J. D., Singh, H. B.,
534 Gregory, G. L., Talbot, R. W., Blake, D. R., and Sachse, G. W.: Origin of ozone and NO_x in the tropical
535 troposphere: A photochemical analysis of aircraft observations over the South Atlantic basin, *J. Geophys.*
536 *Res. Atmos.*, 101, 24235–24250, <https://doi.org/10.1029/96jd00336>, 1996.
- 537 L Laughner, J., Zhu, Q., and Cohen, R. C.: Evaluation of version 3.0B of the BEHR OMI NO₂ product,
538 *Atmos. Meas. Tech.*, 12, 128–146, <https://doi.org/10.5194/amt-12-129-2019>, 2019.
- 539 Lamsal, L. N., Martin, R. V., van Donkelaar, A., Steinbacher, M., Celarier, E. A., Bucsela, E., Dunlea, E.
540 J., and Pinto, J. P.: Ground-level nitrogen dioxide concentrations inferred from the satellite-borne Ozone
541 Monitoring Instrument, *J. Geophys. Res. Atmos.*, 113, 1–15, <https://doi.org/10.1029/2007JD009235>,
542 2008.
- 543 Lamsal, L. N., Martin, R. V., Padmanabhan, A., Van Donkelaar, A., Zhang, Q., Sioris, C. E., Chance, K.,
544 Kurosu, T. P., and Newchurch, M. J.: Application of satellite observations for timely updates to global
545 anthropogenic NO_x emission inventories, *Geophys. Res. Lett.*, 38,
546 <https://doi.org/10.1029/2010GL046476>, 2011.
- 547 Laughner, J. and Cohen, R. C.: Direct observation of changing NO, *Science* (80-.), 366, 723–727, 2019.
- 548 Laughner, J. L., Zhu, Q., and Cohen, R. C.: The Berkeley High Resolution Tropospheric NO₂ product,
549 *Earth Syst. Sci. Data*, 10, 2069–2095, <https://doi.org/10.5194/essd-10-2069-2018>, 2018.
- 550 Li, C., Martin, R. V., Cohen, R. C., Bindle, L., Zhang, D., Chatterjee, D., Weng, H., and Lin, J.: Variable
551 effects of spatial resolution on modeling of nitrogen oxides, *Atmos. Chem. Phys.*, 23, 3031–3049,
552 <https://doi.org/10.5194/acp-23-3031-2023>, 2023a.
- 553 Li, J., Wang, Y., Zhang, R., Smeltzer, C., Weinheimer, A., Herman, J., Boersma, K. F., Celarier, E. A.,
554 Long, R. W., Szykman, J. J., Delgado, R., Thompson, A. M., Knepp, T. N., Lamsal, L. N., Janz, S. J.,
555 Kowalewski, M. G., Liu, X., and Nowlan, C. R.: Comprehensive evaluations of diurnal NO₂
556 measurements during DISCOVER-AQ 2011: Effects of resolution-dependent representation of NO_x
557 emissions, *Atmos. Chem. Phys.*, 21, 11133–11160, <https://doi.org/10.5194/acp-21-11133-2021>, 2021.
- 558 Li, Y., Martin, R. V., Li, C., Boys, B. L., van Donkelaar, A., Meng, J., and Pierce, J. R.: Development and
559 evaluation of processes affecting simulation of diel fine particulate matter variation in the GEOS-Chem
560 model, *Atmos. Chem. Phys.*, 23, 12525–12543, <https://doi.org/10.5194/acp-23-12525-2023>, 2023b.
- 561 Lin, J. T. and McElroy, M. B.: Impacts of boundary layer mixing on pollutant vertical profiles in the
562 lower troposphere: Implications to satellite remote sensing, *Atmos. Environ.*, 44, 1726–1739,
563 <https://doi.org/10.1016/j.atmosenv.2010.02.009>, 2010.
- 564 GMDD - Improved Advection, Resolution, Performance, and Community Access in the New Generation
565 (Version 13) of the High Performance GEOS-Chem Global Atmospheric Chemistry Model (GCHP):
566 <https://gmd.copernicus.org/preprints/gmd-2022-42/>, last access: 18 June 2022.
- 567 Millet, D. B., Baasandorj, M., Farmer, D. K., Thornton, J. A., Baumann, K., Brophy, P., Chaliyakunnel,
568 S., De Gouw, J. A., Graus, M., Hu, L., Koss, A., Lee, B. H., Lopez-Hilfiker, F. D., Neuman, J. A., Paulot,
569 F., Peischl, J., Pollack, I. B., Ryerson, T. B., Warneke, C., Williams, B. J., and Xu, J.: A large and
570 ubiquitous source of atmospheric formic acid, *Atmos. Chem. Phys.*, 15, 6283–6304,



- 571 <https://doi.org/10.5194/acp-15-6283-2015>, 2015.
- 572 Murray, L. T., Jacob, D. J., Logan, J. A., Hudman, R. C., and Koshak, W. J.: Optimized regional and
573 interannual variability of lightning in a global chemical transport model constrained by LIS/OTD satellite
574 data, *J. Geophys. Res. Atmos.*, 117, 1–14, <https://doi.org/10.1029/2012JD017934>, 2012.
- 575 Nault, B. A., Garland, C., Pusede, S. E., Wooldridge, P. J., Ullmann, K., Hall, S. R., and Cohen, R. C.:
576 Measurements of CH₃O₂NO₂ in the upper troposphere, *Atmos. Meas. Tech.*, 8, 987–997,
577 <https://doi.org/10.5194/amt-8-987-2015>, 2015.
- 578 Oak, Y. J., Park, R. J., Schroeder, J. R., Crawford, J. H., Blake, D. R., Weinheimer, A. J., Woo, J. H.,
579 Kim, S. W., Yeo, H., Fried, A., Wisthaler, A., and Brune, W. H.: Evaluation of simulated O₃ production
580 efficiency during the KORUS-AQ campaign: Implications for anthropogenic NO_x emissions in Korea,
581 *Elementa*, 7, <https://doi.org/10.1525/elementa.394>, 2019.
- 582 Reed, A. J., Thompson, A. M., Kollonige, D. E., Martins, D. K., Tzortziou, M. A., Herman, J. R.,
583 Berkoff, T. A., Abuhassan, N. K., and Cede, A.: Effects of local meteorology and aerosols on ozone and
584 nitrogen dioxide retrievals from OMI and Pandora spectrometers in Maryland, USA during DISCOVER-
585 AQ 2011, *J. Atmos. Chem.*, 72, 455–482, <https://doi.org/10.1007/s10874-013-9254-9>, 2015.
- 586 Russell, A. R., Perring, A. E., Valin, L. C., Bucseles, E. J., Browne, E. C., Wooldridge, P. J., and Cohen,
587 R. C.: A high spatial resolution retrieval of NO₂ column densities from OMI: Method and evaluation,
588 *Atmos. Chem. Phys.*, 11, 8543–8554, <https://doi.org/10.5194/acp-11-8543-2011>, 2011.
- 589 Shah, V., Jacob, D., Li, K., Silvern, R., Zhai, S., Liu, M., Lin, J., and Zhang, Q.: Effect of changing
590 NO_x lifetime on the seasonality and long-term trends of satellite-observed tropospheric NO₂ columns
591 over China, *Atmos. Chem. Phys.*, 20, 1483–1495, <https://doi.org/10.5194/acp-20-1483-2020>, 2020.
- 592 Shah, V., Jacob, D. J., Dang, R., Lamsal, L. N., Strode, S. A., Steenrod, S. D., Boersma, K. F., Eastham,
593 S. D., Fritz, T. M., Thompson, C., Peischl, J., Bourgeois, I., Pollack, I. B., Nault, B. A., Cohen, R. C.,
594 Campuzano-Jost, P., Jimenez, J. L., Andersen, S. T., Carpenter, L. J., Sherwen, T., and Evans, M. J.:
595 Nitrogen oxides in the free troposphere: Implications for tropospheric oxidants and the interpretation of
596 satellite NO₂ measurements, *Atmos. Chem. Phys.*, 23, 1227–1257, [https://doi.org/10.5194/acp-23-1227-](https://doi.org/10.5194/acp-23-1227-2023)
597 2023, 2023.
- 598 Simone, N. W., Stettler, M. E. J., and Barrett, S. R. H.: Rapid estimation of global civil aviation emissions
599 with uncertainty quantification, *Transp. Res. Part D Transp. Environ.*, 25, 33–41,
600 <https://doi.org/10.1016/j.trd.2013.07.001>, 2013.
- 601 Van Stratum, B. J. H., Vilá-Guerau De Arellano, J., Ouwersloot, H. G., Van Den Dries, K., Van Laar, T.
602 W., Martinez, M., Lelieveld, J., Diesch, J. M., Drewnick, F., Fischer, H., Hosaynali Beygi, Z., Harder, H.,
603 Regelin, E., Sinha, V., Adame, J. A., Sörgel, M., Sander, R., Bozem, H., Song, W., Williams, J., and
604 Yassaa, N.: Case study of the diurnal variability of chemically active species with respect to boundary
605 layer dynamics during DOMINO, *Atmos. Chem. Phys.*, 12, 5329–5341, [https://doi.org/10.5194/acp-12-](https://doi.org/10.5194/acp-12-5329-2012)
606 5329-2012, 2012.
- 607 Tao, Y., Huang, W., Huang, X., Zhong, L., Lu, S. E., Li, Y., Dai, L., Zhang, Y., and Zhu, T.: Estimated
608 acute effects of ambient ozone and nitrogen dioxide on mortality in the Pearl River Delta of southern
609 China, *Environ. Health Perspect.*, 120, 393–398, <https://doi.org/10.1289/ehp.1103715>, 2012.
- 610 Thornton, J. A., Wooldridge, P. J., and Cohen, R. C.: Atmospheric NO₂: In Situ laser-induced
611 fluorescence detection at parts per trillion mixing ratios, *Anal. Chem.*, 72, 528–539,
612 <https://doi.org/10.1021/ac9908905>, 2000.
- 613 Tong, L., Zhang, H., Yu, J., He, M., Xu, N., Zhang, J., Qian, F., Feng, J., and Xiao, H.: Characteristics of



- 614 surface ozone and nitrogen oxides at urban, suburban and rural sites in Ningbo, China, *Atmos. Res.*, 187,
615 57–68, <https://doi.org/10.1016/j.atmosres.2016.12.006>, 2017.
- 616 Valin, L. C., Russell, A. R., Hudman, R. C., and Cohen, R. C.: Effects of model resolution on the
617 interpretation of satellite NO₂ observations, *Atmos. Chem. Phys.*, 11, 11647–11655,
618 <https://doi.org/10.5194/acp-11-11647-2011>, 2011.
- 619 Vandaele, A. C., Hermans, C., Fally, S., Carleer, M., Colin, R., Mérienne, M. F., Jenouvrier, A., and
620 Coquart, B.: High-resolution Fourier transform measurement of the NO₂ visible and near-infrared
621 absorption cross sections: Temperature and pressure effects, *J. Geophys. Res. Atmos.*, 107, ACH 3-1-
622 ACH 3-12, <https://doi.org/10.1029/2001JD000971>, 2002.
- 623 Veefkind, J. P., Aben, I., McMullan, K., Förster, H., de Vries, J., Otter, G., Claas, J., Eskes, H. J., de
624 Haan, J. F., Kleipool, Q., van Weele, M., Hasekamp, O., Hoogeveen, R., Landgraf, J., Snel, R., Tol, P.,
625 Ingmann, P., Voors, R., Kruizinga, B., Vink, R., Visser, H., and Levelt, P. F.: TROPOMI on the ESA
626 Sentinel-5 Precursor: A GMES mission for global observations of the atmospheric composition for
627 climate, air quality and ozone layer applications, *Remote Sens. Environ.*, 120, 70–83,
628 <https://doi.org/10.1016/j.rse.2011.09.027>, 2012.
- 629 Verhoelst, T., Compernelle, S., Pinardi, G., Lambert, J. C., Eskes, H. J., Eichmann, K. U., Fjæraa, A. M.,
630 Granville, J., Niemeijer, S., Cede, A., Tiefengraber, M., Hendrick, F., Pazmiño, A., Bais, A., Bazureau,
631 A., Folkert Boersma, K., Bogner, K., Dehn, A., Donner, S., Elokhov, A., Gebetsberger, M., Goutail, F.,
632 Grutter De La Mora, M., Gruzdev, A., Gratsea, M., Hansen, G. H., Irie, H., Jepsen, N., Kanaya, Y.,
633 Karagkiozidis, D., Kivi, R., Kreher, K., Levelt, P. F., Liu, C., Müller, M., Navarro Comas, M., Piders, A.
634 J. M., Pommereau, J. P., Portafaix, T., Prados-Roman, C., Puentedura, O., Querel, R., Remmers, J.,
635 Richter, A., Rimmer, J., Cárdenas, C. R., De Miguel, L. S., Sinyakov, V. P., Stremme, W., Strong, K.,
636 Van Roozendaal, M., Pepijn Veefkind, J., Wagner, T., Wittrock, F., Yela González, M., and Zehner, C.:
637 Ground-based validation of the Copernicus Sentinel-5P TROPOMI NO₂ measurements with the NDACC
638 ZSL-DOAS, MAX-DOAS and Pandonia global networks, *Atmos. Meas. Tech.*, 14, 481–510,
639 <https://doi.org/10.5194/amt-14-481-2021>, 2021.
- 640 Weng, H., Lin, J., Martin, R., Millet, D. B., Jaeglé, L., Ridley, D., Keller, C., Li, C., Du, M., and Meng,
641 J.: Global high-resolution emissions of soil NO_x, sea salt aerosols, and biogenic volatile organic
642 compounds, *Sci. Data*, 7, 1–15, <https://doi.org/10.1038/s41597-020-0488-5>, 2020.
- 643 Yang, L. H., Jacob, D. J., Dang, R., Oak, Y. J., Lin, H., Kim, J., Zhai, S., Colombi, N. K., Pendergrass, D.
644 C., Beaudry, E., Shah, V., Feng, X., Yantosca, R. M., Chong, H., Park, J., Lee, H., Lee, W.-J., Kim, S.,
645 Kim, E., Travis, K. R., Crawford, J. H., and Liao, H.: Interpreting GEMS geostationary satellite
646 observations of the diurnal variation of nitrogen dioxide (NO₂) over East Asia, *EGUsphere*, 1–25, 2023a.
- 647 Yang, L. H., Jacob, D. J., Colombi, N. K., Zhai, S., Bates, K. H., Shah, V., Beaudry, E., Yantosca, R. M.,
648 Lin, H., Brewer, J. F., Chong, H., Travis, K. R., Crawford, J. H., Lamsal, L. N., Koo, J. H., and Kim, J.:
649 Tropospheric NO₂ vertical profiles over South Korea and their relation to oxidant chemistry: implications
650 for geostationary satellite retrievals and the observation of NO₂ diurnal variation from space, *Atmos.*
651 *Chem. Phys.*, 23, 2465–2481, <https://doi.org/10.5194/acp-23-2465-2023>, 2023b.
- 652 Zhang, D., Martin, R. V., Bindle, L., Li, C., Eastham, S. D., van Donkelaar, A., and Gallardo, L.:
653 Advances in Simulating the Global Spatial Heterogeneity of Air Quality and Source Sector Contributions:
654 Insights into the Global South, *Environ. Sci. Technol.*, 57, 6955–6964,
655 <https://doi.org/10.1021/acs.est.2c07253>, 2023.
- 656 Zhang, Y., Wang, Y., Chen, G., Smeltzer, C., Crawford, J., Olson, J., Szykman, J., Weinheimer, A. J.,
657 Knapp, D. J., Montzka, D. D., Wisthaler, A., Mikoviny, T., Fried, A., and Diskin, G.: *Journal of*
658 *Geophysical Research : Atmospheres of DISCOVER-AQ 2011 observations*, 1–13,



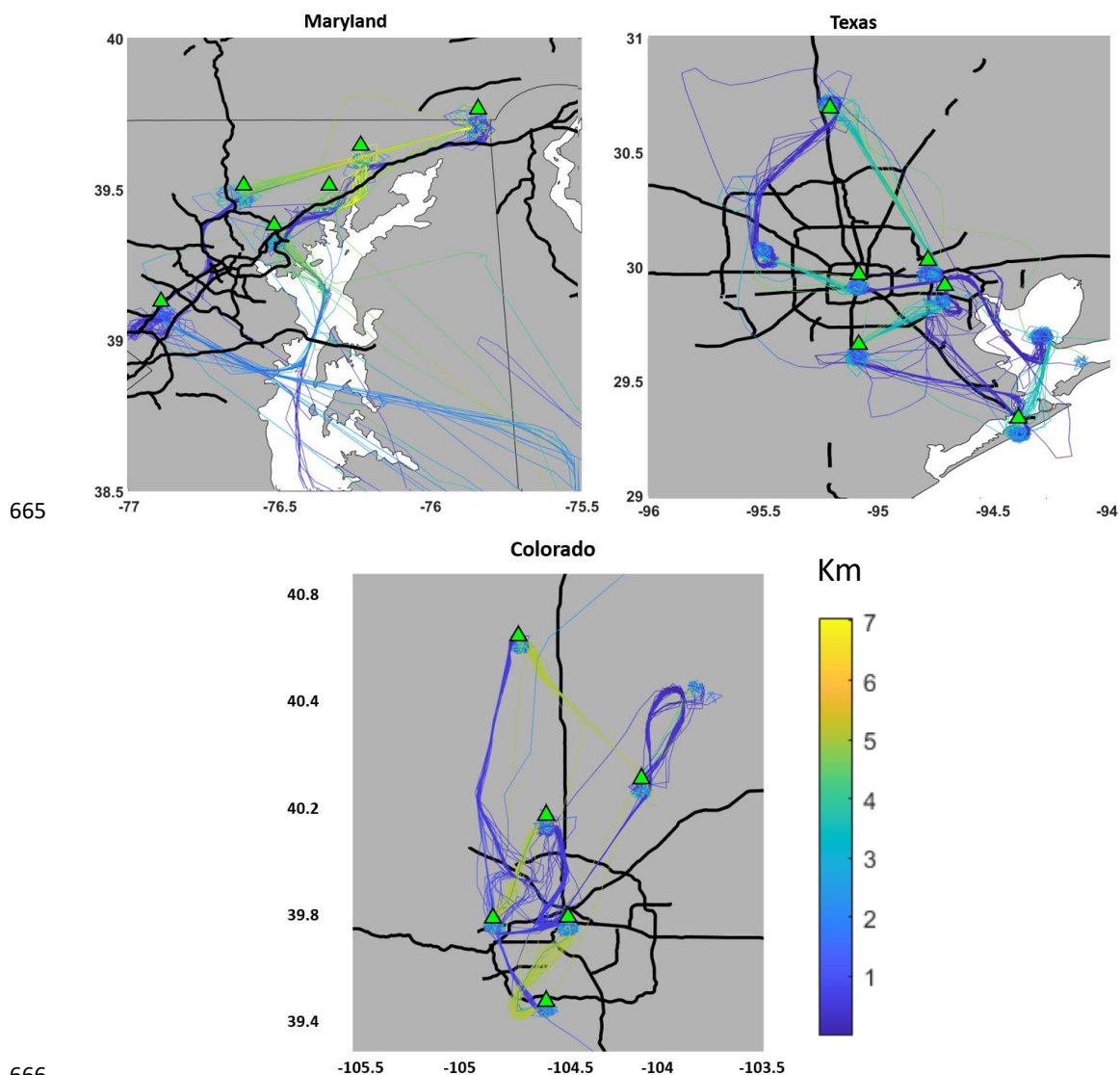
659 <https://doi.org/10.1002/2015JD024203>.Received, 2016.

660 Zhao, X., Fioletov, V., Cede, A., Davies, J., and Strong, K.: Accuracy, precision, and temperature
661 dependence of Pandora total ozone measurements estimated from a comparison with the Brewer triad in
662 Toronto, Atmos. Meas. Tech., 9, 5747–5761, <https://doi.org/10.5194/amt-9-5747-2016>, 2016.

663

664

Appendix

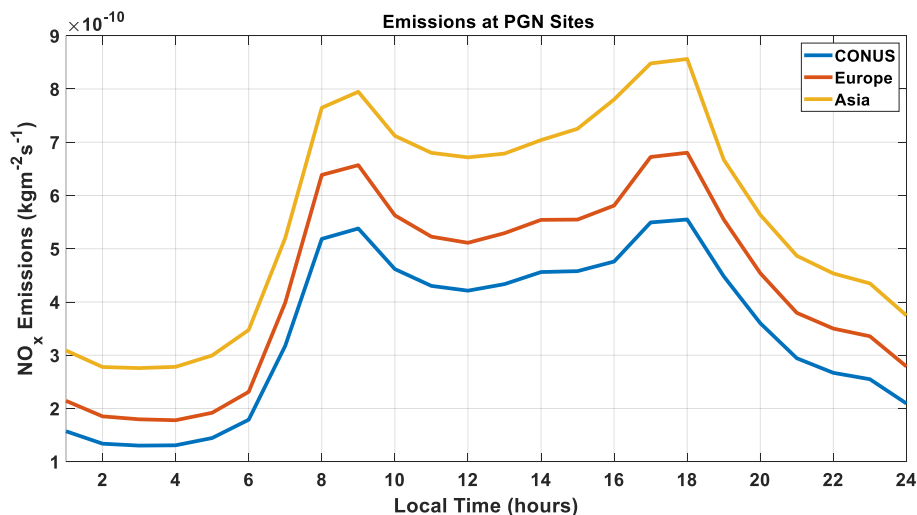


666

667



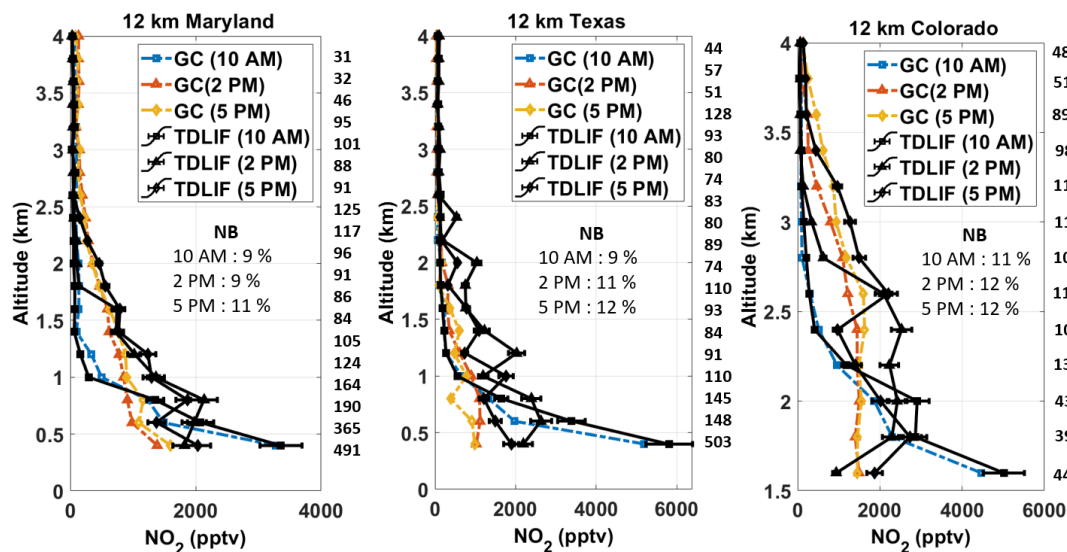
668 Figure A1. Flight tracks showing the path and altitude of the P-3B aircraft during the DISCOVER-AQ
 669 campaign over Maryland during July 2011 (left), over Texas during September 2013 (center) and Colorado
 670 (right). The green triangles show the locations of the Pandora sun photometers that have been used in this
 671 study. The Sites names and coordinates are listed in Table A1. Grey indicates land, white indicates water.
 672 The black bold lines indicate roads.



673

674 Figure A2. Hourly variation of NO_x emissions including all sectors across 50 PGN sites over the CONUS,
 675 Europe, and east Asia.

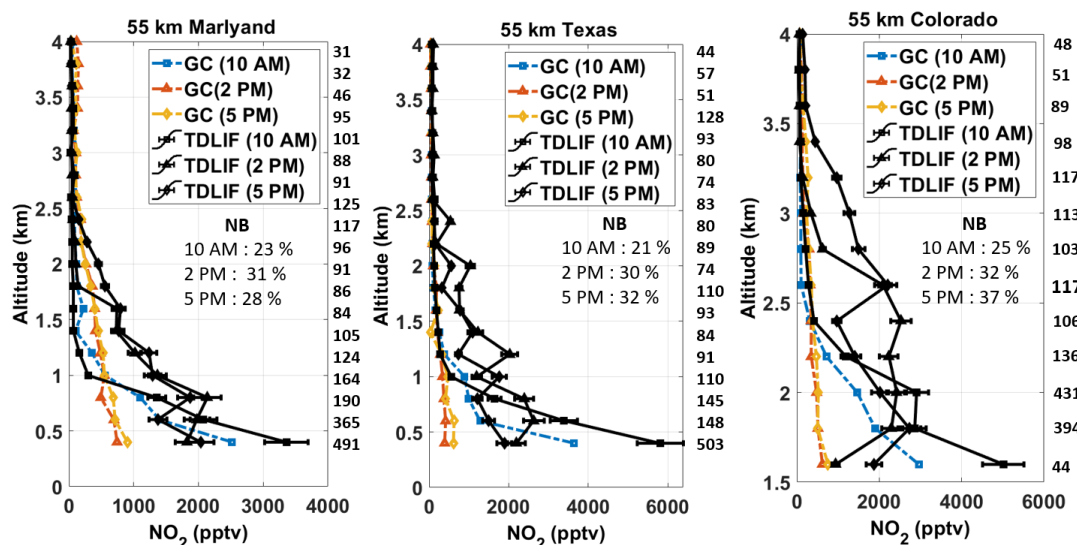
676



677

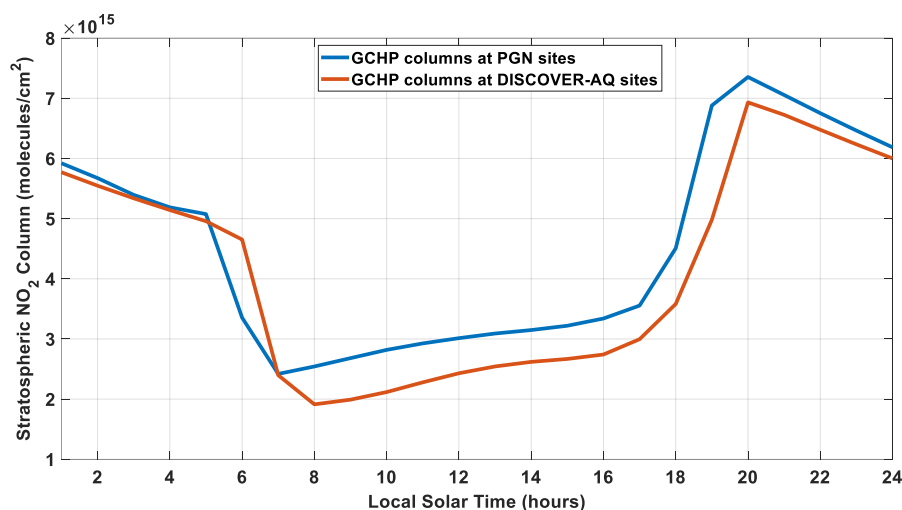


678 Figure A3: NO₂ Vertical profiles from TD-LIF instrument aboard during the DISCOVER-AQ campaign
 679 over Maryland, Texas and Colorado. The black lines represent observations (square: 10 AM, triangle: 2
 680 PM, diamond: 5 PM). The colored lines represent GCHP 12 km simulated NO₂ mixing ratios without
 681 modifying the PBLH (blue: 10 AM, orange: 2 PM, yellow: 5 PM). The inset values in the boxes show the
 682 NB at 10 AM, 2 PM, and 5 PM. The numbers in the middle represent the number the observations associated
 683 with the corresponding altitude level. Error bars indicate standard errors in measurements.



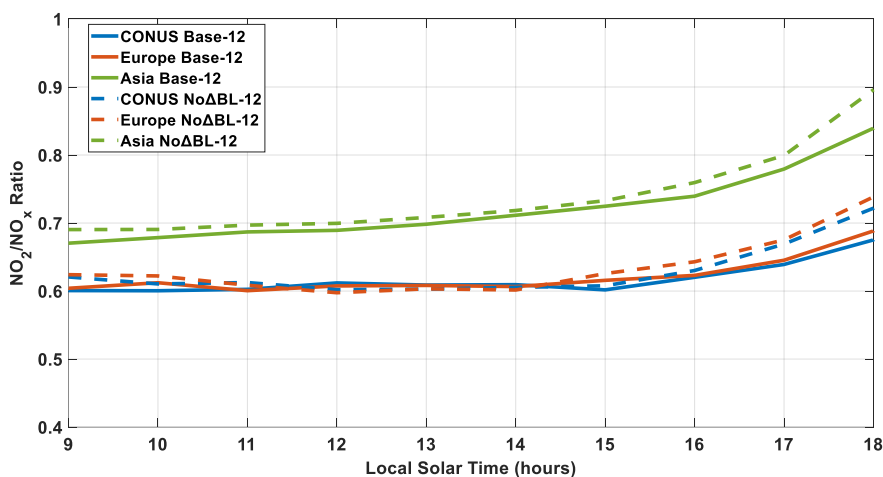
684

685 Figure A4: NO₂ Vertical profiles from TD-LIF instrument aboard during the DISCOVER-AQ campaign
 686 over Maryland, Texas and Colorado. The black lines represent observations (square: 10 AM, triangle: 2
 687 PM, diamond: 5 PM). The colored lines represent GCHP 55 km simulated NO₂ mixing ratios without
 688 modifying the PBLH (blue: 10 AM, orange: 2 PM, yellow: 5 PM). The inset values in the boxes show the
 689 NB at 10 AM, 2 PM, and 5 PM. The numbers in the middle represent the number the observations associated
 690 with the corresponding altitude level. Error bars indicate standard errors in measurements.



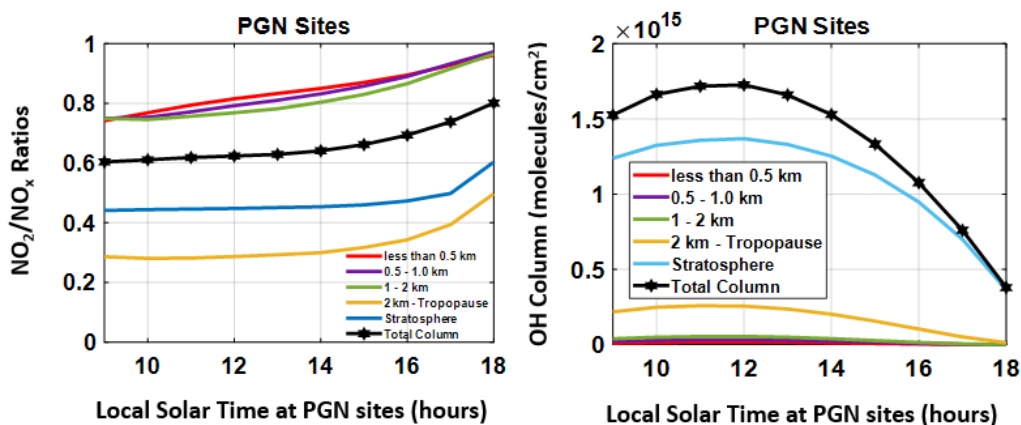
691

692 Figure A5. GCHP NO₂ stratospheric columns for the three-month average of June-July-August at
693 DISCOVER-AQ sites (red) and PGN sites (blue).



694

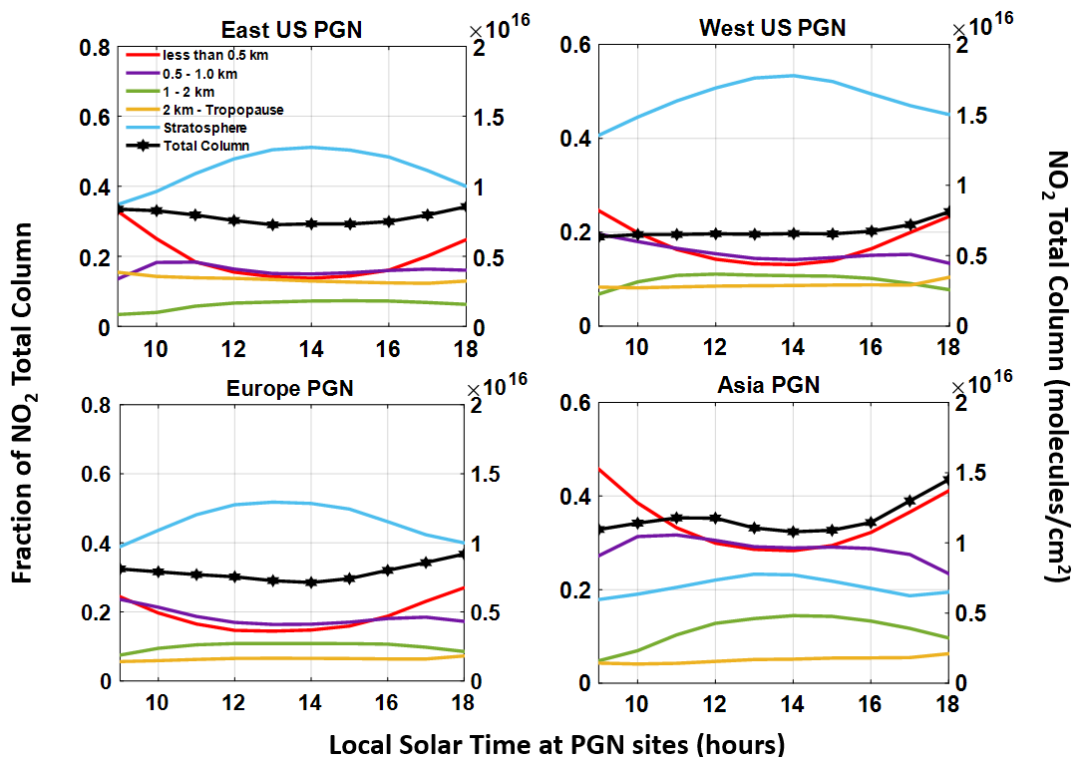
695 Figure A6. Hourly variation of 12 km simulated column NO₂/NO_x ratios across 50 PGN sites over the
696 CONUS (red), Europe (blue), and east Asia (green). The dotted lines show the 12 km simulated NO₂/NO_x
697 ratios without modified PBLH.



698

699 Figure A7. Simulated NO_2/NO_x ratios (left panel) and simulated partial and total OH columns (right panel)
 700 at different hours of the day averaged over the summer months of June-July-August for 2019 for PGN sites
 701 over the eastern US, western US, Europe, and eastern Asia.

702



703

704 Figure A8. The simulated fractional contribution of NO_2 columns at different hours of the day averaged
 705 over the summer months of June-July-August for 2019 for PGN sites over the eastern US, western US,
 706 Europe, and eastern Asia. The right Y-axis shows the total columns of NO_2 .



707

708 Table A1. Site name, latitude and longitude for 18 sites in Texas, Maryland, and Colorado that has
709 concurrent pandora and aircraft measurements.

710

711	Site	Sites name	Latitude	Longitude	Date
712		Texas Sites			September 2013
713	1.	Channelview	29.802	95.125	
714	2.	Conroe	30.350	95.425	
715	3.	Deer Park	29.670	95.128	
716	4.	Galveston	29.254	95.861	
717	5.	Manvel Croix	29.520	95.392	
718	6.	Moody Tower	29.718	95.341	
719		Maryland Sites			July 2011
720	1.	Aldino	39.563	76.204	
721	2.	Beltsville	39.055	76.878	
722	3.	Edgewood	39.410	76.297	
723	4.	Essex	39.311	76.474	
724	5.	Fairhill	39.701	75.860	
725	6.	Padonia	39.461	76.631	
726		Colorado Sites			July-August 2014
727	1.	Bao Tower	40.043	105.012	
728	2.	Chatfield Park	39.535	105.074	
729	3.	Denver La Casa	39.782	105.018	
730	4.	Fort Collins	40.595	105.143	
731	5.	Platteville	40.183	104.734	
732	6.	NREL-Golden	39.743	105.181	

733

734 Table A2. Site name, latitude and longitude for 31 sites in CONUS and 11 sites in Europe, North
735 Africa and Middle-east, and 9 sites in east Asia from the PGN database.



736

Site	Site Name	Latitude	Longitude	Date
	Eastern US			June-July-August 2019
1.	'Bristol_PA'	40.1074	-74.8824	
2.	'Cambridge_MA'	42.3800	-71.1100	
3.	'CapeElizabeth_ME'	43.5610	-70.2073	
4.	'ChapelHill_NC'	35.9708	-79.0933	
5.	'CharlesCity_VA'	37.3260	-77.2057	
6.	'Dearborn_MI'	42.3067	-83.1488	
7.	'Detroit_MI.txt'	42.3026	-83.1068	
8.	'Hampton_VA'	37.0203	-76.3366	
9.	'Londonderry_NH'	42.8625	-71.3801	
10.	'Lynn_MA'	42.4746	-70.9708	
11.	'Madison_CT'	41.2568	-72.5533	
12.	'Manhattan_NY'	40.8153	-73.9505	
13.	'NewBrunswick_NJ'	40.4622	-74.4294	
14.	'NewHaven_CT'	41.3014	-72.9029	
15.	'OldField_NY'	40.9635	-73.1402	
16.	'Philadelphia_PA'	39.9919	-75.0811	
17.	'Pittsburgh_PA '	40.4655	-79.9608	
18.	'WallopsIsland_VA '	37.8439	-75.4775	
19.	'WashingtonDC'	38.9218	-77.0124	
20.	'Westport_CT'	41.1183	-73.3367	



Western US			June-July-August 2019
21.	'Aldine_TX'	29.9011	-95.3262
22.	'Boulder_CO'	40.0375	-105.2420
23.	'Edwards_CA '	34.9600	-117.8811
24.	'Houston_TX'	29.7200	-95.3400
25.	'LaPorte_TX'	29.6721	-95.0647
26.	'Manhattan_KS'	39.1022	-96.6096
27.	'MountainView_CA'	37.4200	-122.05680
28.	'Richmond_CA'	37.9130	-122.3360
29.	'SaltLakeCity_UT'	40.7663	-111.8478
30.	'SouthJordan_UT'	40.5480	-112.0700
31.	'Wrightwood_CA'	34.3819	-117.6813
Europe			June-July-August 2019
32.	'Athens'	37.9878	23.7750
33.	'Bremen'	53.0813	8.8126
34.	'Brussels'	50.7980	4.3580
35.	'Cologne'	50.9389	6.9787
36.	'Davos'	46.8000	9.8300
37.	'Innsbruck'	47.2643	11.3852
38.	'Juelich'	50.9080	6.4130
39.	'Lindenberg'	52.2900	14.1200
40.	'Rome'	42.1057	12.6402
41.	'Tel-Aviv'	32.1129	34.8062



		Eastern Asia		June-July-August 2019	
42.	'Beijing'	40.0048	116.3786		
43.	'Kobe'	34.7190	135.2900		
44.	'Sapporo'	43.0727	141.3459		
45.	'Seosan'	36.7769	126.4938		
46.	'Seoul'	37.5644	126.9340		
47.	'Tokyo'	35.6200	139.3834		
48.	'Tsukuba'	36.0661	140.1244		
49.	'Ulsan'	35.5745	129.1896		
50.	'Yokosuka'	35.3207	139.6508		

737

738 Table A3. Sectoral contribution to NO_x emissions averaged over all PGN sites, the US, Europe
739 and Asia.

PGN Sites	TRA(%)	RCO(%)	IND(%)	ENE(%)	SHP(%)	AGR(%)	WST(%)
ALL	49	19	13	7	7	4	1
CONUS	45	29	16	4	2	3	1
Europe	47	11	8	10	16	7	1
Asia	55	12	15	9	4	3	2

740

741 TRA: Transport, RCO: Residential Combustion, IND: Industry, ENE: Energy, SHP: Ship Emissions, AGR:
742 Agriculture, WST: Waste

743